Flexible, Foldable, Actively Multiplexed, High-Density Electrode Array for Mapping Brain Activity *in vivo*

Jonathan Viventi[1,2⊥], Dae-Hyeong Kim[3⊥], Leif Vigeland[4], Eric S. Frechette[5], Justin A. Blanco[6], Yun-Soung Kim[7], Andrew E. Avrin[8], Vineet R. Tiruvadi[9], Suk-Won Hwang[7], Ann C. Vanleer[9], Drausin F. Wulsin[9], Kathryn Davis[5], Casey E. Gelber[9], Larry Palmer[4], Jan Van der Spiegel[8], Jian Wu[10], Jianliang Xiao[11], Yonggang Huang[12], Diego Contreras[4], John A. Rogers[7], Brian Litt[5,9*]

[1]*Department of Electrical and Computer Engineering, Polytechnic Institute of New York University, Brooklyn, NY 11201 USA*

[2]*Center for Neural Science, New York University, New York, NY 10003 USA*

[3]*School of Chemical and Biological Engineering, Seoul National University, Seoul 151-744 Korea*

[4]*Department of Neuroscience, University of Pennsylvania School of Medicine, 215 Stemmler Hall, Philadelphia, PA 19104 USA*

[5]*Department of Neurology, Hospital of the University of Pennsylvania, 3 West Gates, 3400 Spruce Street, Philadelphia, PA 19104 USA*

[6]*Department of Electrical and Computer Engineering, United States Naval Academy, Annapolis, MD 21402 USA*

[7]*Department of Materials Science and Engineering, Beckman Institute for Advanced Science and Technology and Frederick Seitz Materials Research Laboratory, University of Illinois at Urbana-Champaign, Urbana, Illinois 61801 USA*

[8]*Department of Electrical and Systems Engineering, University of Pennsylvania, Philadelphia, PA 19104 USA*

[9]*Department of Bioengineering, University of Pennsylvania, Philadelphia, PA 19104 USA*

[10]*AML, Department of Engineering Mechanics, Tsinghua Univeristy, Beijing 100084, China*

[11]*Department of Mechanical Engineering, University of Colorado Boulder, Boulder, CO 80309 USA*

[12]*Departments of Civil and Environmental Engineering and Mechanical Engineering, Northwestern University, Evanston, IL 60208*

[⊥] *J. Viventi and D.-H. Kim contributed equally.*

*To whom correspondence should be addressed. *E-mail:* littb@mail.med.upenn.edu; jrogers@uiuc.edu

Online Methods

Fabrication of the Active Electrode Array

Doped silicon nano-ribbons on a silicon-on-insulator (SOI) wafer (Si(260 nm)/SiO_2(1000 nm)/Si; SOITEC, France) were prepared using a high temperature diffusion process (950-1000 °C) in a rapid thermal annealing (RTA) system. These nano-ribbons were transfer printed onto a PI substrate (12.5 μm, Kapton, Dupont, USA) using spin-coated, uncured polyimide (PI) as a glue layer. Once the PI is cured, gate oxide is deposited with plasma enhanced chemical vapour deposition (PECVD, plasmatherm, USA). Contact openings for the source and drain connects are made with a buffered oxide etchant (BOE, Transene, USA). Finally, metal (Cr/Au, 5nm/150nm) is deposited using an electron beam evaporator (Temescal, USA), creating n-type transistor arrays. Each unit cell contains 2 transistors, which are connected by metal lines. Subsequent layers of metal interconnections are electrically isolated with polymeric inter-layer dielectric (1.2 μm, polyimide, Sigma Aldrich, USA). Following two metal circuit interconnection layers, a

water-proof encapsulation is formed with a photocurable epoxy (SU8, Microchem Corp), protecting the device while submerged in conductive bio-fluids. The completed active sensor array is connected to an interface circuit board through a flexible anisotropic conductive film (ACF, elform, USA).

Multiplexing

The connections between four unit cells are illustrated in **Supplementary Figure 15**. When connected to an external constant current sink the selected unit cell completes the current path from +V to –V and forms a source-follower amplifier. The buffered voltage output is from the same circuit node that is connected to the constant current sink. The 18 row select signals of the multiplexed electrode array were cycled at 5 kHz to sample all of the electrodes on the array, yielding a sampling rate of ~277 Hz per active electrode, with all 18 electrodes in a given column sampled sequentially. The multiplexer output settles in less than 5 μS, allowing the row select signals to be cycled at > 200 kHz. With faster analog to digital converters, the electrode sampling rate can be readily increased to > 10 kS/s per electrode without loss of SNR[27], as validated using an analog to digital converter capable of sampling at 1 MS/s.

Data Acquisition

The multiplexed analog signals were synchronously sampled at 100 kS/s using a custom data acquisition system (see **Supplementary Figs. 16 – 25** and supplemental material online). 20 times oversampling per switch interval was used to improve the SNR (yielding the 5 kHz cycling rate previously stated). Voltage data were recorded from all

360 electrodes of the active electrode array. The reference (ground) electrode for the acquisition system was clipped to nearby, exposed muscle. Except where otherwise indicated, the μECOG data for all experiments were band-pass filtered from 1 to 50 Hz using a 6th order butterworth band-pass filter in the forward and reverse directions, resulting in zero-phase distortion digital filtering (and effectively doubling the order of the filter to a 12^{th} order filter).

Animal Experiments

Experiments were conducted in accordance with the ethical guidelines of the National Institutes of Health and with the approval of the Institutional Animal Care and Use Committee of the University of Pennsylvania. Surgical and stimulation methods were as described in detail previously[51],[52]. Briefly, adult cats (2.5-3.5 kg) were anesthetized with intravenous thiopental with a continuous infusion (3-10 mg/kg/hr) and paralyzed with gallamine triethiodide (Flaxedil). Heart rate, blood pressure, end-tidal CO_2 and EEG were monitored throughout the experiment to assure depth and stability of anesthesia and rectal temperature was kept at 37-38°C with a heating pad. The surface of the visual cortex was exposed with a craniotomy centered at Horsley Clarke posterior 4.0, lateral 2.0.

During visual stimulation, the corneas were protected with contact lenses after dilating the pupils with 1% ophthalmic atropine and retracting the nictitating membranes with phenylephrine (Neosynephrine). Spectacle lenses were chosen by the tapetal reflection technique to optimize the focus of stimuli on the retina. The position of the monitor was adjusted with an x-y-stage so that the areae centrals were centered on the screen. Stimuli were presented on an Image Systems (Minnetonka, MN) model M09LV

monochrome monitor operating at 125 frames per second at a spatial resolution of 1024 × 786 pixels and a mean luminance of 47 cd/m^2.

Bending Stiffness and Bending Strain

The cross section of the electrode array is shown in **Supplementary Figure 1b**. Since the Au (500 nm and 150 nm), Si (260 nm) and SiO_2 (100 nm) layers between the top SU8 and bottom Kapton are very thin, and are very close to the neutral mechanical plane, their contribution to the bending stiffness can be approximated by polyimide (PI) within 1% error. Therefore the complex multilayer electrode can be approximated by a two-layer structure, composed of PI of thickness h_2 and SU8 of thickness h_1. The distance of neutral mechanical plane from the Kapton bottom is y_0, and is obtained as

$$y_0 = \frac{1}{2}\frac{\overline{E}_{PI}h_2^2 + \overline{E}_{SU8}h_1(2h_2 + h_1)}{\overline{E}_{PI}h_2 + \overline{E}_{SU8}h_1}. \tag{S1}$$

where $\overline{E}_i = \frac{E_i}{1-v_i^2}$ relates to Young's modulus E_i and Poisson's ratio v_i (i=*PI* for PI layer, i=*SU8* for SU8 layer).

The bending stiffness of the electrode is

$$EI = \overline{E}_{PI}bh_2\left(\frac{1}{3}h_2^2 - h_2y_0 + y_0^2\right) + \overline{E}_{SU8}bh_1\left[\frac{1}{3}h_1^2 + h_1(h_2 - y_0) + (h_2 - y_0)^2\right], \tag{S2}$$

where b=10 mm is the electrode width.

For the electrode bent to a radius of R, the strain at position of distance y from the Kapton bottom is

$$\varepsilon = \frac{y - y_0}{R}. \tag{S3}$$

Mechanics of Electrode Insertion

The electrode is folded around a soft PDMS of Young's modulus $E_{PDMS} = 100\,kPa$, width B and thickness h_{PDMS}, and is inserted into the gap of thickness h_{gap} between the hemispheres of the brain. The insertion depth is d (see **Supplementary Fig. 26a**). Since the thickness of brain (>10 mm) is much larger than that of the folded electrode (~ 0.7 mm), the two hemispheres of the brain are modeled as semi-infinite solids, of Young's modulus E_{brain} =3 kPa and Poisson's ratio ν_{brain} =0.35 [53]. For a semi-infinite solid subject to uniform pressure p at the top surface in the circular region of radius $a = \sqrt{Bd}$, the surface subsidence w at position of distance r from the circular center is $w = \left[4(1-\nu_{brain}^2)\,p\sqrt{Bd}\right] \Big/ \left(\pi E_{brain}\right) \int_0^{\pi/2} \sqrt{1 - r^2 \sin^2\varphi / (Bd)}\, d\varphi$, whose average over the pressure region is obtained as

$$\overline{w} = \frac{16(1-\nu_{brain}^2)\,p\sqrt{Bd}}{3\pi E_{brain}}. \tag{S4}$$

Since the electrode array is much stiffer and thinner than PDMS, its deformation due to insertion is negligible compared to PDMS. Therefore, displacement continuity gives the relation between the pressure at the interface p and the average subsidence $\overline{w}$ of the brain surface due to electrode insertion to be $\frac{p}{E_{PDMS}} h_{PDMS} + 2\overline{w} = h_{PDMS} - h_{gap}$, which gives

$$p = \frac{h_{PDMS} - h_{gap}}{\dfrac{h_{PDMS}}{E_{PDMS}} + \dfrac{32(1-\nu_{brain}^2)\sqrt{Bd/\pi}}{3\pi E_{brain}}}. \tag{S5}$$

And the maximum compressive strain in the brain due to electrode insertion is obtained as

$$\varepsilon^{\max} = \frac{-(1+\nu_{brain})p}{E_{brain}}\left[1-2\nu_{brain}+2\left(\frac{2\nu_{brain}}{3}\right)^{\frac{3}{2}}\right]$$
$$= \frac{-(1+\nu_{brain})\left[1-2\nu_{brain}+2\left(\frac{2\nu_{brain}}{3}\right)^{\frac{3}{2}}\right]\left(h_{PDMS}-h_{gap}\right)\cdot}{\left[\frac{E_{brain}}{E_{PDMS}}h_{PDMS}+\frac{32\left(1-\nu_{brain}^2\right)\sqrt{Bd}}{3\pi^{3/2}}\right]\sqrt{}} \quad \text{(S6)}$$

As the folded electrode inserts into the brain gap (insertion length *d*), the gap h_{gap} between the left and right brains decreases and approaches an asymptote $\overline{h}_{gap}$ (i.e., minimal gap distance). The brain gap h_{gap} can be generally written as an exponentially decaying function of the rubber insertion length *d*, $h_{gap} = \overline{h}_{gap} + \left(h_{PDMS} - \overline{h}_{gap}\right)\exp\left(-d/1mm\right)$, which defines zero insertion length as rubber first touches the brain (i.e., $h_{gap} = h_{PDMS}$). For $h_{PDMS} = 700\ \mu m$ and *B*=16.2mm in experiment, the maximum compressive strain in the brain versus the insertion depth of rubber is shown in **Supplementary Figure 26b** for minimal brain gaps $\overline{h}_{gap}$ = 500 and 600 μm.

Circuit Design

The dimensions of the two transistors in the unit-cell (**Fig. 1b**, left frame) are equal so that they will have matched performance. The width of both transistors was chosen to be as large as possible at 200 μm while still leaving room for large interconnections between adjacent unit cells. The L was chosen at 20 μm to be conservative for the

processing technology. The resulting W/L ratio of 10 yielded reasonable levels of current output. The width of all metal lines and size of all VIAs was increased by 2 ~ 4× from prior designs to improve reliability and ease manufacturing. The electrode spacing was set at 500 μm based on prior work and to match well with the 500 μm spacing of the ACF ribbon cable, enabling a simple layout of the interconnections.

Current Sinks

The ideal current sinks shown in **Supplementary Figure 15** can be implemented using commercially available semiconductors as shown in the block diagram in **Supplementary Figure 17**. This basic circuit that is implemented 20 times, one for each column of the electrode array. The circuit makes use of several commercial semiconductors. The first of which is the LM334 which is a 3-Terminal Adjustable Current Source (National Semiconductor). It is used to set the constant current for the source follower. The current is adjusted via a potentiometer on the third pin (not shown). The constant current generated by the LM334 is mirrored by the current mirror section of the REF200 – Current Reference (Texas Instruments). The REF200 is used because the LM334 cannot respond to fast transients while supplying low amounts of current. The REF200 current mirror bandwidth is 5 MHz, to enable fast multiplexing. The REF200 also contains two 100 μA constant current sources, which are not used.

The output of a single column from the electrode array is connected to the current mirror and the non-inverting input of a TLC2274 Op Amp as shown. The TLC2274 Op Amp (Texas Instruments) is used to provide buffering for the output of the source follower amplifier. This op-amp buffers the signal before the high pass filter. Additionally,

adding this op-amp allows the buffering to occur as close as possible to the electrode array, minimizing parasitic capacitance and maximizing the switching speed.

The output of the Op Amp is connected to a 0.01 Hz high-pass filter. This very low frequency high pass filter is used to remove the average DC offset introduced by the source follower configuration of the amplifiers on the electrode array. The high pass filter frequency must be very low because it introduces aliasing for signals up to ~0.1 Hz. Signals lower than this present on one multiplexed channel will be aliased onto the other channels. However, any aliasing that occurs can be removed by a subsequent 1 Hz digital high pass filter on the acquired data.

Data Acquisition System

The output of the high pass filter is connected using a short cable (2') to a custom data acquisition system interface (see **Supplementary Figs. 16b**, **c** and **Supplementary Figs. 18 – 25**). The signal will be buffered again by another TLC2274 op-amp to drive the 15' cable from the acquisition system interface board to a set of four PXI-6289 data acquisition cards (National Instruments, USA). This second stage of buffering prevents any loading introduced by the long cable run from influencing the high pass filter stage.

The data acquisition system is controlled through custom LabVIEW software (National Instruments). The data are demultiplexed in software, in real-time. The first and last sample in a given multiplexer switch interval are discarded since these samples are adjacent to the row select signal transition and usable due to timing inaccuracies in the PXI-6289 analog to digital converter. If an over-sampling ratio (OSR) greater than 3 is used, the samples that remain after discarding the first and last samples are averaged in real-time,

further reducing the recorded noise. A subset of the demultiplexed channels is shown in real-time during the experiment. All data are saved for later offline filtering and analysis using custom MATLAB software (The MathWorks).

Gain

The gain of the electrode array was measured by submerging the array in conductive saline. A second electrode was submerged in the saline approximately 1" from the electrode array. The second electrode was connected to a 100 mV peak to peak sine wave at 3.14 Hz. This test presents a uniform signal for all of the electrodes on the array to measure. The recording duration of this test was 80 seconds and the sampling rate was ~277 Hz per electrode. The median signal level for all 360 channels on the array was 68 mV peak to peak, yielding a median gain of 0.68. The gain of the array can be increased to ~1 with improvements to the biasing circuitry off of the electrode array. Significant voltage gain is possible with alternative circuit designs.

The spatial distribution of the peak to peak amplitudes measured is shown in **Supplementary Figure 27** illustrating the uniformity of the gain across the electrode array. ~83% of the electrode channels were operational for this sample. Channels that were determined to be not operational through this test were interpolated from neighboring operational channels using a 2-D averaging spatial filter of window size 3 x 3 pixels prior to all of the analyses presented in the main text.

Power supplies

This electrode array design does not require symmetric power supplies. That is, the +V supply does not need to be equal and opposite of the –V supply. In fact, the source follower amplifier only requires that the +V supply is greater than V_{in}, the input voltage minus V_t, the threshold voltage of the amplifying transistor. Given that V_{in} is typically within the range +/- 100 mV for neural signals, as long as V_t is greater than +100 mV (typical values are ~0.7 V, **Fig. 1b**, center frame), +V can be directly connected to ground (0V). However, if V_t of the array is small or negative, the +V supply can be connected to a separate, small positive voltage supply, such as 0.5V.

Directly connecting the array +V connection to GND or at least minimizing the voltage of the positive supply has several advantages. The most important of which is that it reduces the potential for leakage currents through the gate of the buffer transistor (**Fig. 1b**, left frame) by reducing the voltage potential between the electrode (gate) and the silicon substrate. Another advantage is simplifying the power connections for the electrode array.

Electrode Materials

The electrode base metal is gold and an additional coating of flat platinum has been added to reduce the electrode impedance. Passive electrodes sized 250 μm × 250 μm using the same dimensions and materials processing steps were fabricated to measure the impedance difference. Passive electrodes must be used to measure the impedance because it is not currently possible to measure electrode impedance while integrated in the active electrode.

The mean impedance of the 250 μm × 250 μm passive electrodes was 84 kOhm ± 17% at 1 kHz, while the impedance of the same electrode design coated with flat platinum was 29 kOhm ± 9% at 1 kHz. Measurements were conducted with the array immersed in normal saline (0.9%). The reduced impedance provided by the platinum coating should increase the current output of the electrode and enable better signal transfer.

The electrodes in the active electrode array illustrated in **Fig. 1a** are 300 μm × 300 μm. Based on linear extrapolation from prior measurements, we expect the impedance of these electrodes to be ~69% of the measured value (29 kOhm) of the 250 μm × 250 μm electrodes or ~20 kOhm at 1 kHz.

The output impedance of the active electrodes are significantly lower than 20 kOhm due to the integrated buffer amplifier which allows the multiplexer to settle rapidly after switching, despite driving large parasitic capacitances due to long interface cabling.

SI Figure Captions

Supplementary Figure 1. Schematic of fabrication steps **a,** Microscope images of each fabrication step. **b,** schematic cross-sectional information, red dotted line shows the location of neutral mechanical plane (NMP).

Supplementary Figure 2. A single-trial visual evoked potential from a full-field drifting grating. **a,** Spatial distribution of the visual evoked response, as determined by the root-mean-square (RMS) value of the zero-meaned signal within the 40 ms to 160 ms window after the stimulus. Data are anatomically orientated as shown in the inset of **Figure 3b**. **b,** Individual visual evoked responses shown for the 49 electrodes located in the bottom, left-hand corner of the electrode array, as highlighted by the dashed box above.

Supplementary Figure 3. Analysis of the frequency content of a sustained, counter-clockwise spiral during a short seizure. The primary frequency component was 6 Hz. The power spectral density was calculated using 'pwelch' with a window size of 1024 on each channel of the electrode array individually. The resulting power spectra were averaged to produce a single overall power spectral density.

Supplementary Figure 4 – 14. Delay maps for all of the spikes in each cluster indicated a strong similarity within clusters. The spikes in clusters 2, 4, 12, 14, and 19 appeared to occur almost exclusively during seizures, while spikes in the other clusters appeared to occur uniformly throughout the record.

Supplementary Figure 15. Circuit diagram of four unit cells, showing multiplexing connections.

Supplementary Figure 16. Photographs of data acquisition system components. **a,** Photograph of custom circuit board that implements the off array constant current sinks, buffering and high-pass filtering. **b,** Photograph of custom data acquisition interface circuit board that generates row select signals and provides another stage of buffering (top) and **c,** (bottom).

Supplementary Figure 17. Block diagram of constant current sink implementation. This circuit is repeated 20 times, one for each column of the electrode array.

Supplementary Figures 18 – 25. Complete schematics of the custom data acquisition interface circuit board.

Supplementary Figure 26. Folded electrode mechanical modeling results. **a,** A diagram that shows parameter definitions for insertion model of folded electrode array. **b,** Strain induced in the brain during insertion of the folded electrode array for two different brain hemisphere spacings.

Supplementary Figure 27. Color map illustrating the spatial distribution of the electrode response to a 100mV p-p, 3.14 Hz sine wave, demonstrating the spatial uniformity of the gain of the electrode array.

Supplementary Movie 1. Movie of a short electrographic seizure showing numerous complicated spatial patterns, including clockwise and counterclockwise spiral waves. The

voltage for all 360 channels is plotted as a color map in the top of the frame, while the average of all 360 electrodes is plotted at the bottom of the frame with a vertical bar indicating the position in time for reference. The movie is presented ~18× slower than real-time. (MPEG; 29.3 MB).

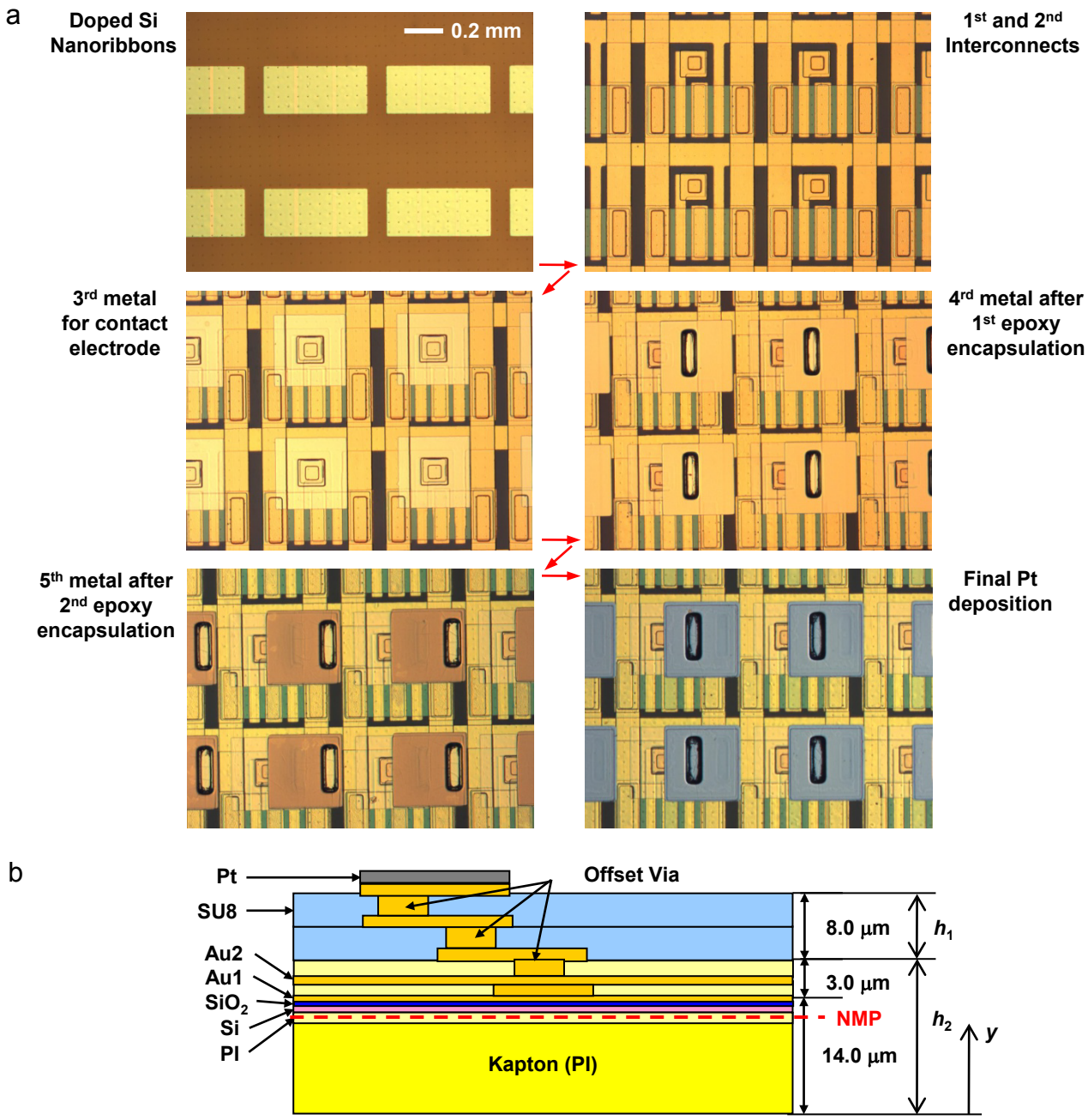

Supplementary Figure 1. Schematic of fabrication steps **a,** Microscope images of each fabrication step. **b,** schematic cross-sectional information, red dotted line shows the location of neutral mechanical plane (NMP).

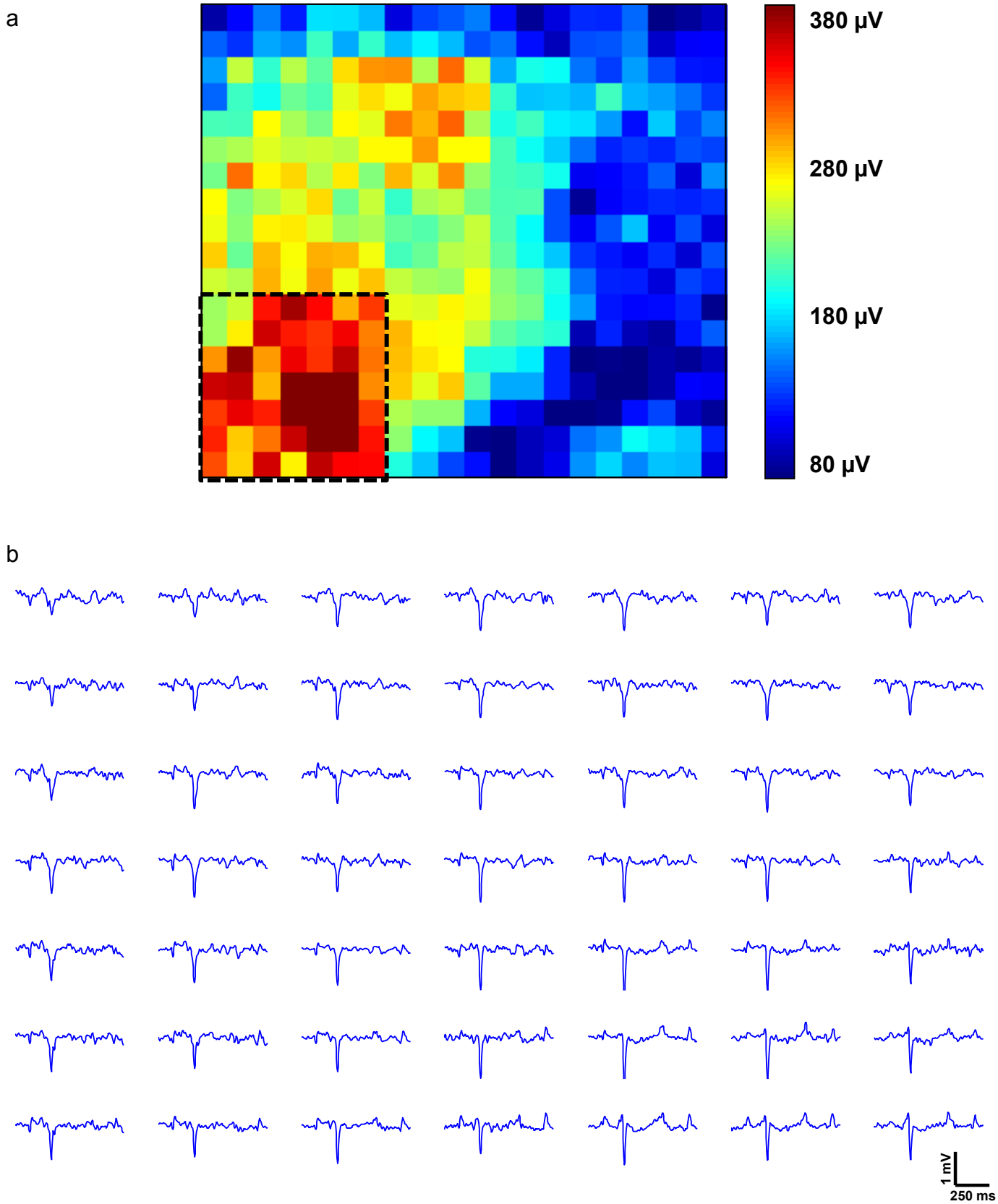

Supplementary Figure 2. A single-trial visual evoked potential from a full-field drifting grating. **a,** Spatial distribution of the visual evoked response, as determined by the root-mean-square (RMS) value of the zero-meaned signal within the 40 ms to 160 ms window after the stimulus. Data are anatomically orientated as shown in the inset of **Figure 3b**. **b,** Individual visual evoked responses shown for the 49 electrodes located in the bottom, left-hand corner of the electrode array, as highlighted by the dashed box above.

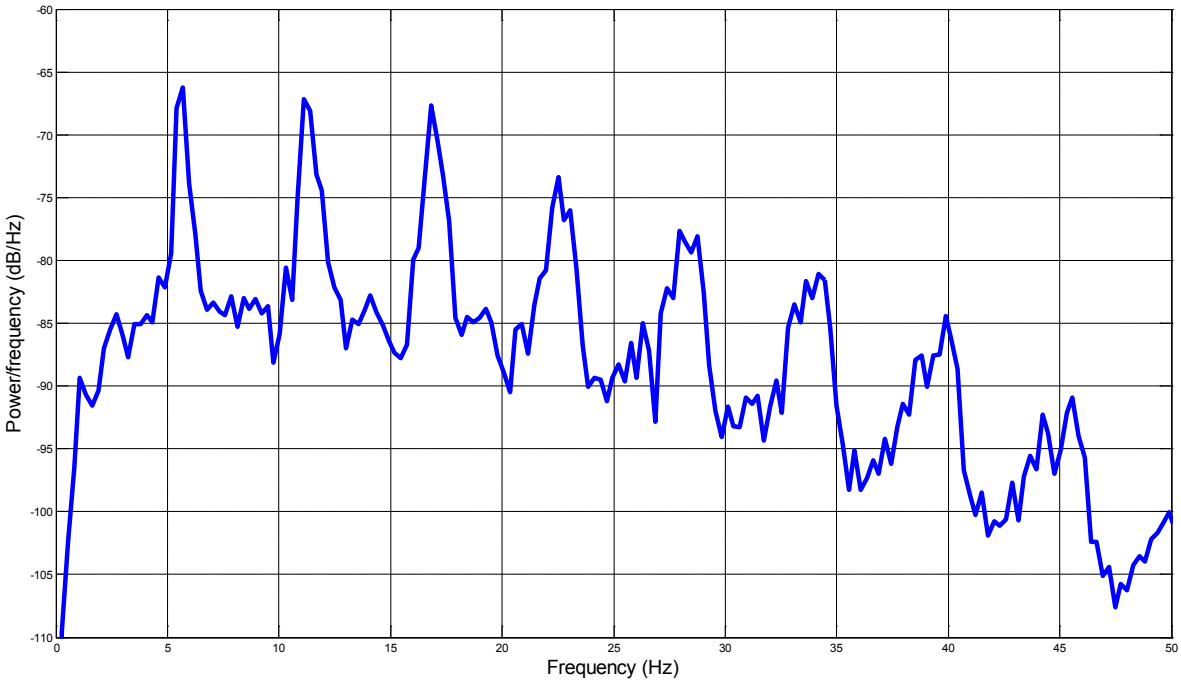

Supplementary Figure 3. Analysis of the frequency content of a sustained, counter-clockwise spiral during a short seizure. The primary frequency component was 6 Hz. The power spectral density was calculated using 'pwelch' with a window size of 1024 on each channel of the electrode array individually. The resulting power spectra were averaged to produce a single overall power spectral density.

a

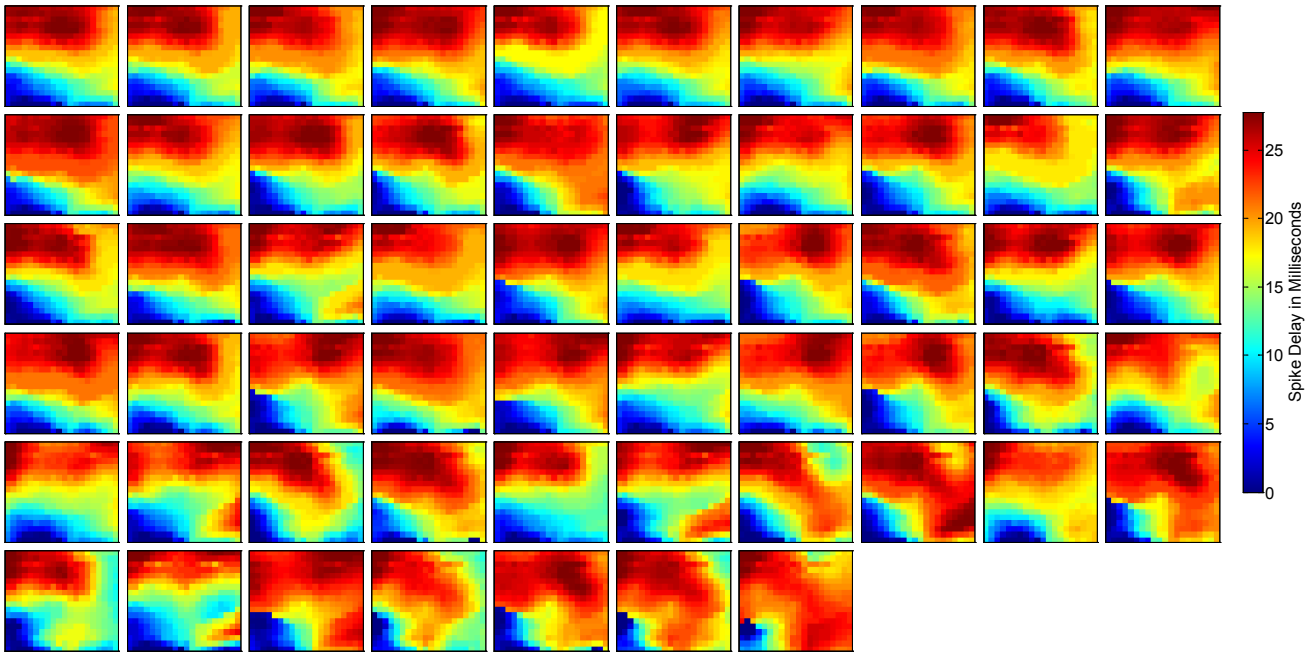

b

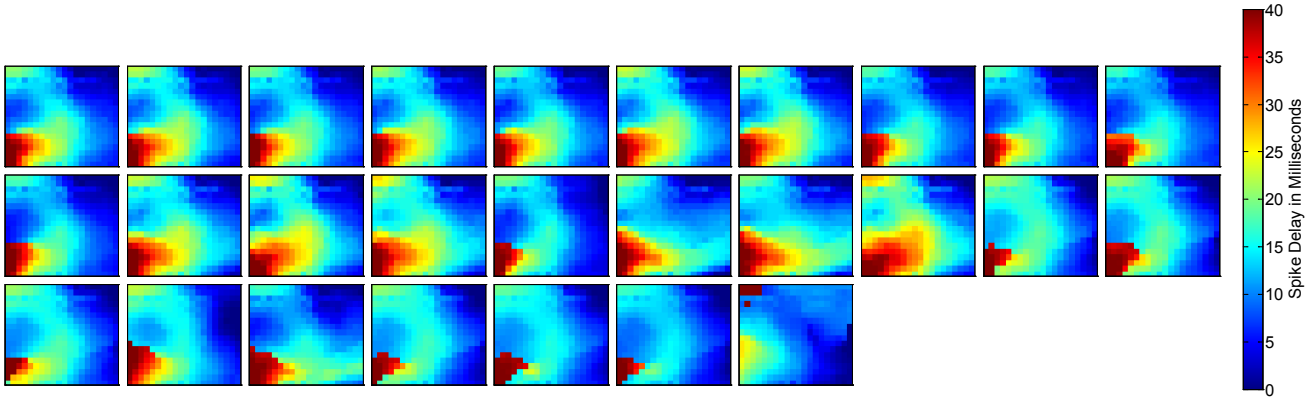

Supplementary Figure 4. Delay maps for all of the spikes in each cluster indicated a strong similarity within clusters. The spikes in clusters 2, 4, 12, 14, and 19 appeared to occur almost exclusively during seizures, while spikes in the other clusters appeared to occur uniformly throughout the record.

a

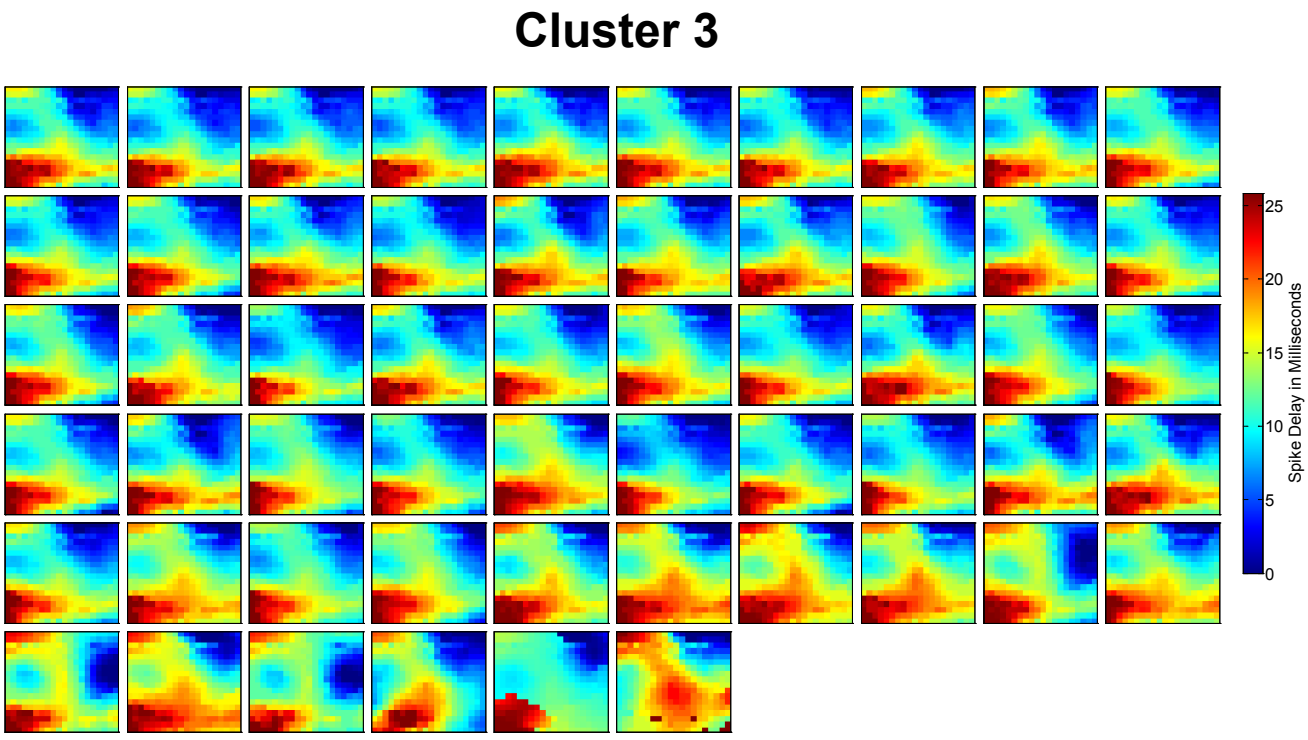

b

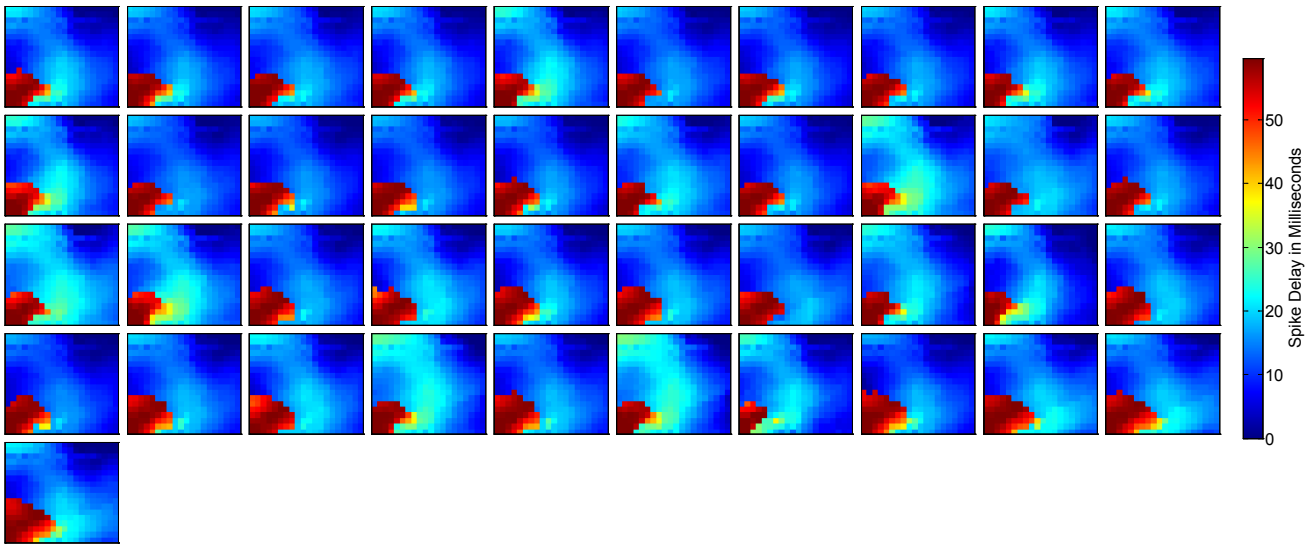

Supplementary Figure 5. Delay maps for all of the spikes in each cluster indicated a strong similarity within clusters. The spikes in clusters 2, 4, 12, 14, and 19 appeared to occur almost exclusively during seizures, while spikes in the other clusters appeared to occur uniformly throughout the record.

a

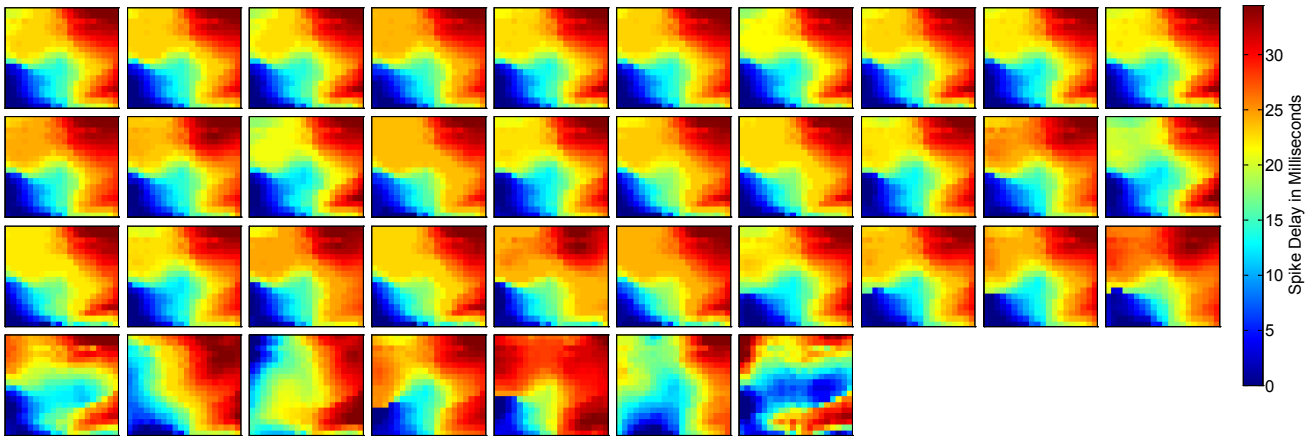

b

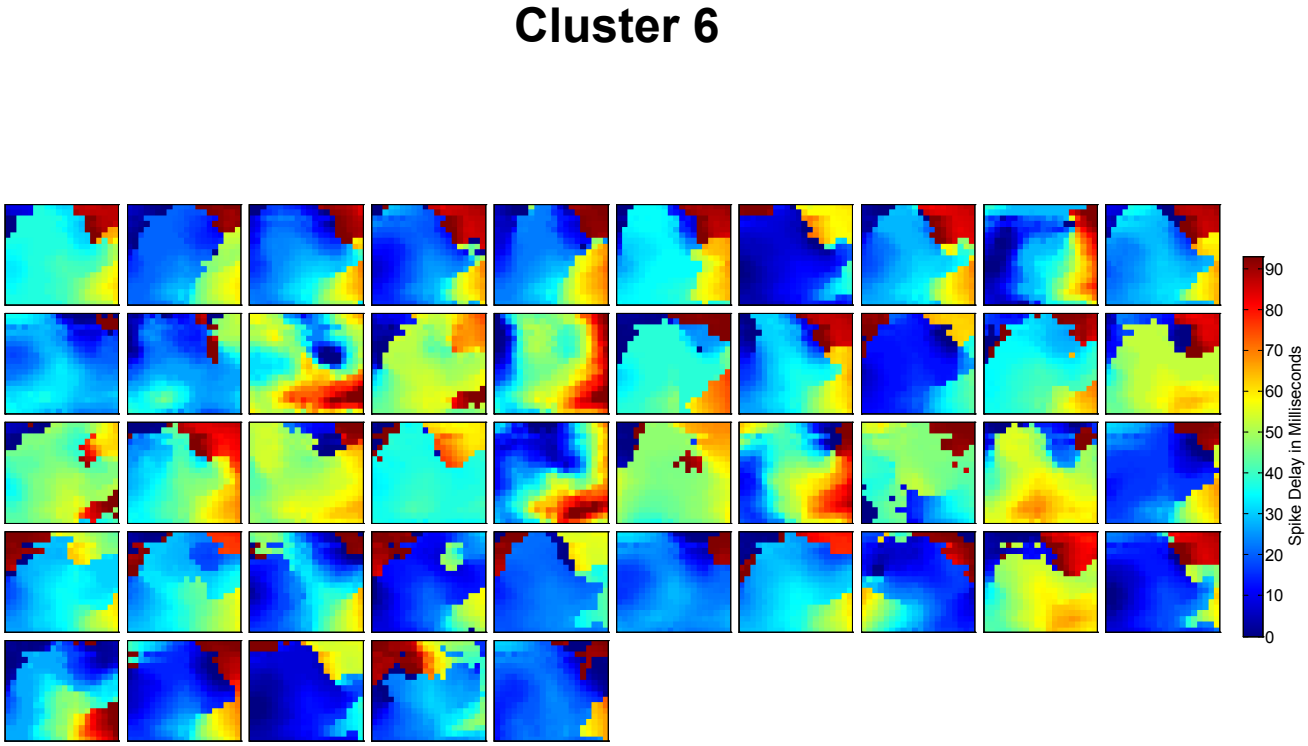

Supplementary Figure 6. Delay maps for all of the spikes in each cluster indicated a strong similarity within clusters. The spikes in clusters 2, 4, 12, 14, and 19 appeared to occur almost exclusively during seizures, while spikes in the other clusters appeared to occur uniformly throughout the record.

a

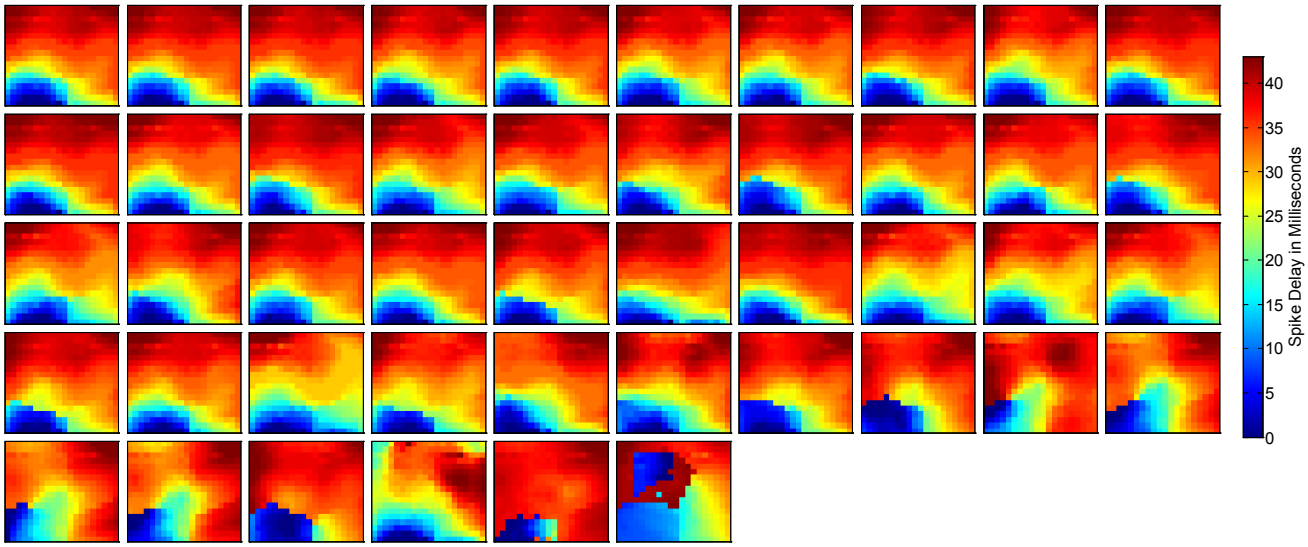

b

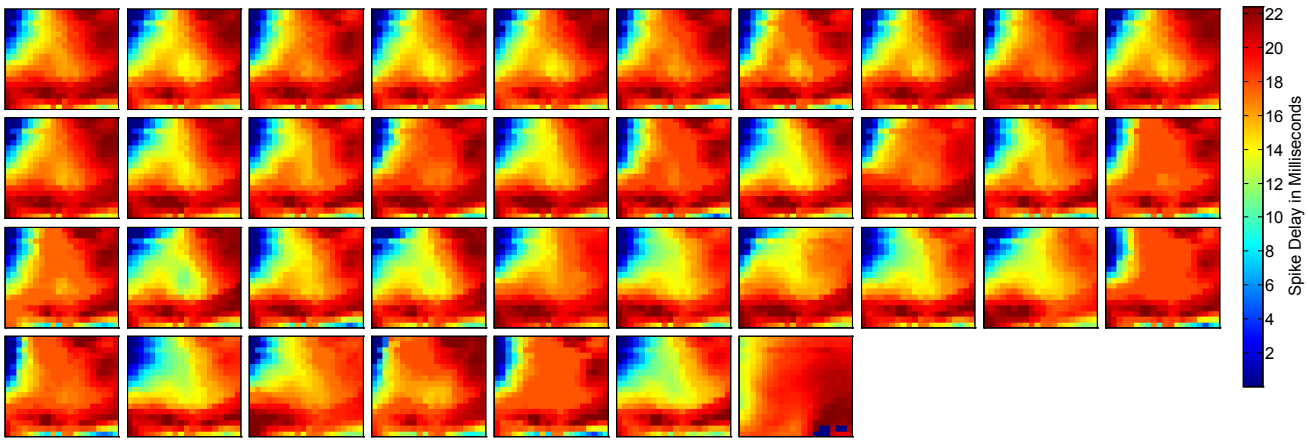

Supplementary Figure 7. Delay maps for all of the spikes in each cluster indicated a strong similarity within clusters. The spikes in clusters 2, 4, 12, 14, and 19 appeared to occur almost exclusively during seizures, while spikes in the other clusters appeared to occur uniformly throughout the record.

a

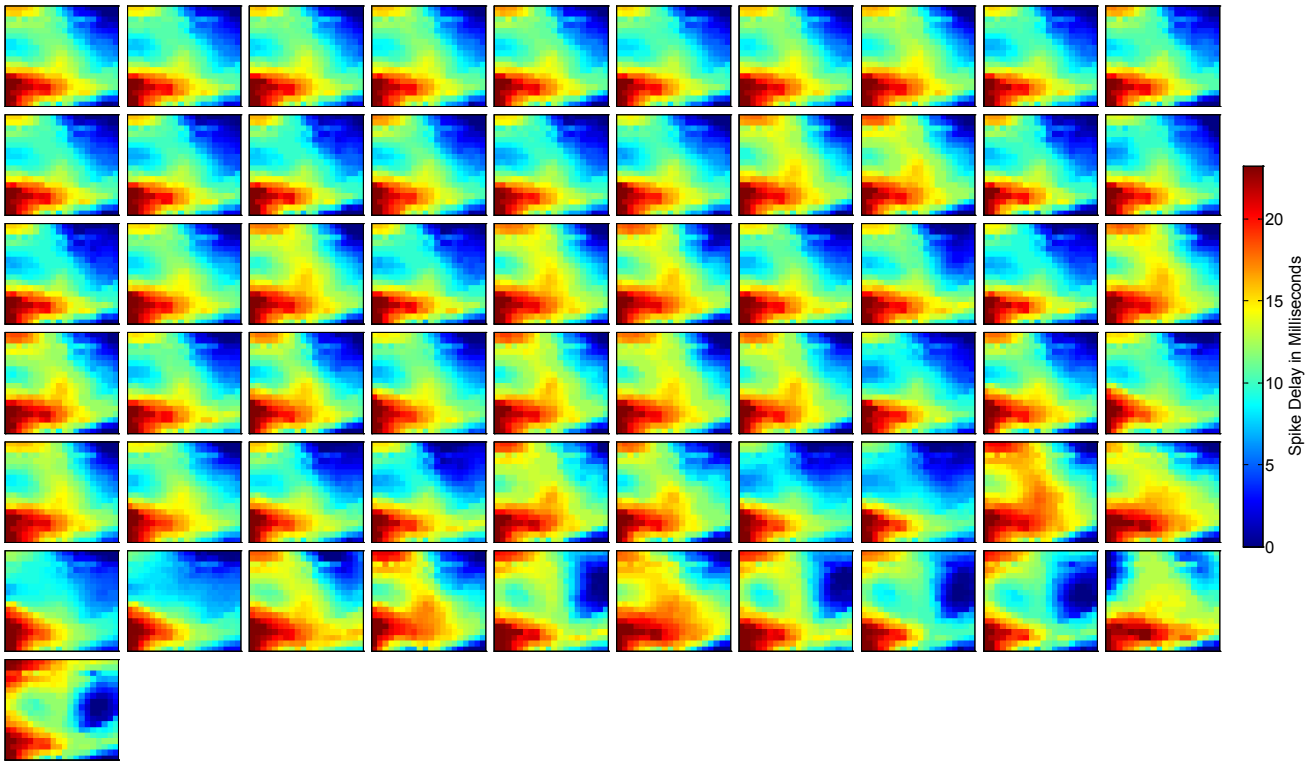

b

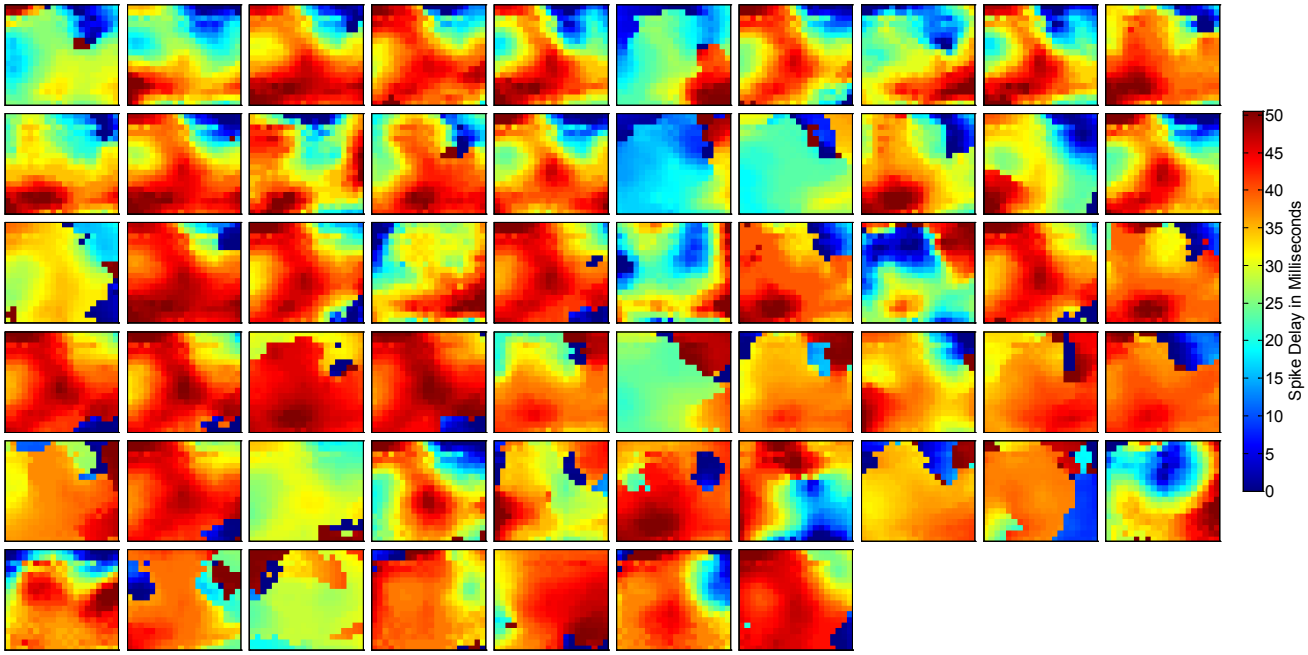

Supplementary Figure 8. Delay maps for all of the spikes in each cluster indicated a strong similarity within clusters. The spikes in clusters 2, 4, 12, 14, and 19 appeared to occur almost exclusively during seizures, while spikes in the other clusters appeared to occur uniformly throughout the record.

a

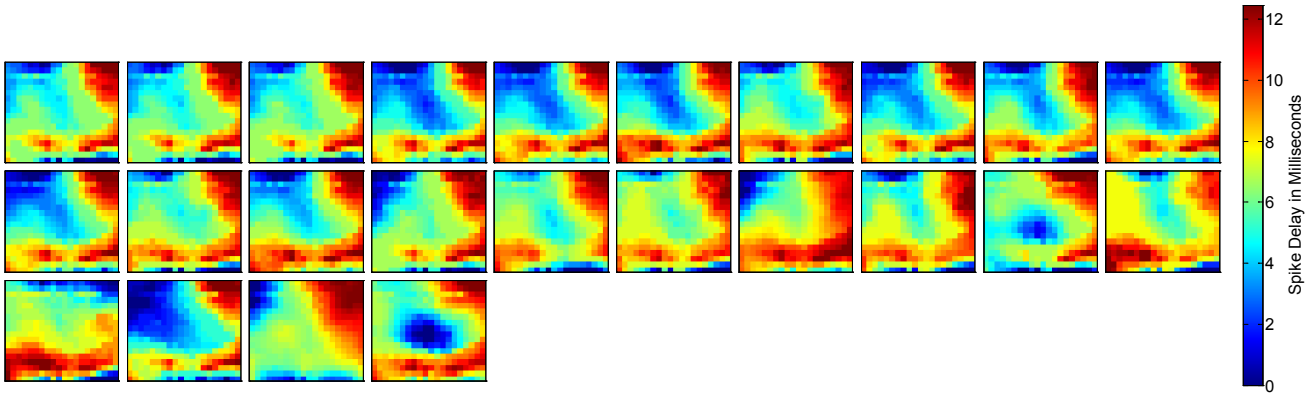

b

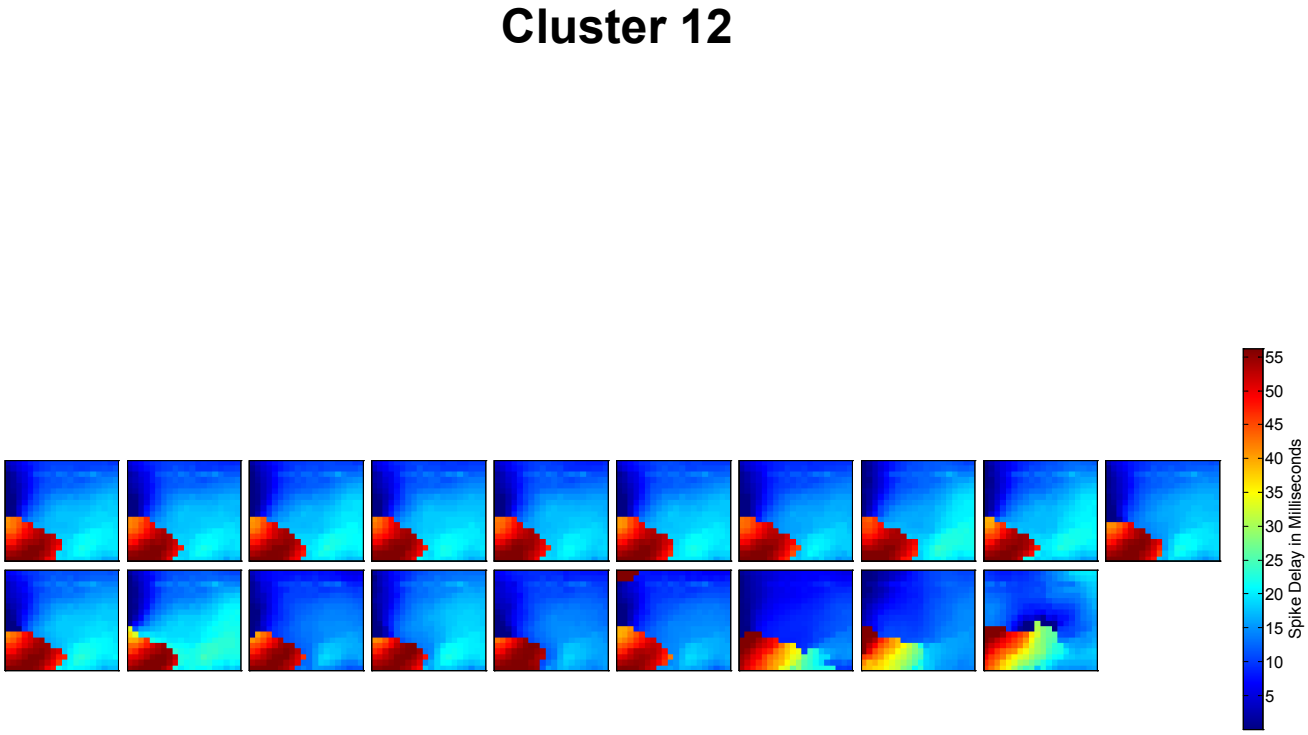

Supplementary Figure 9. Delay maps for all of the spikes in each cluster indicated a strong similarity within clusters. The spikes in clusters 2, 4, 12, 14, and 19 appeared to occur almost exclusively during seizures, while spikes in the other clusters appeared to occur uniformly throughout the record.

a

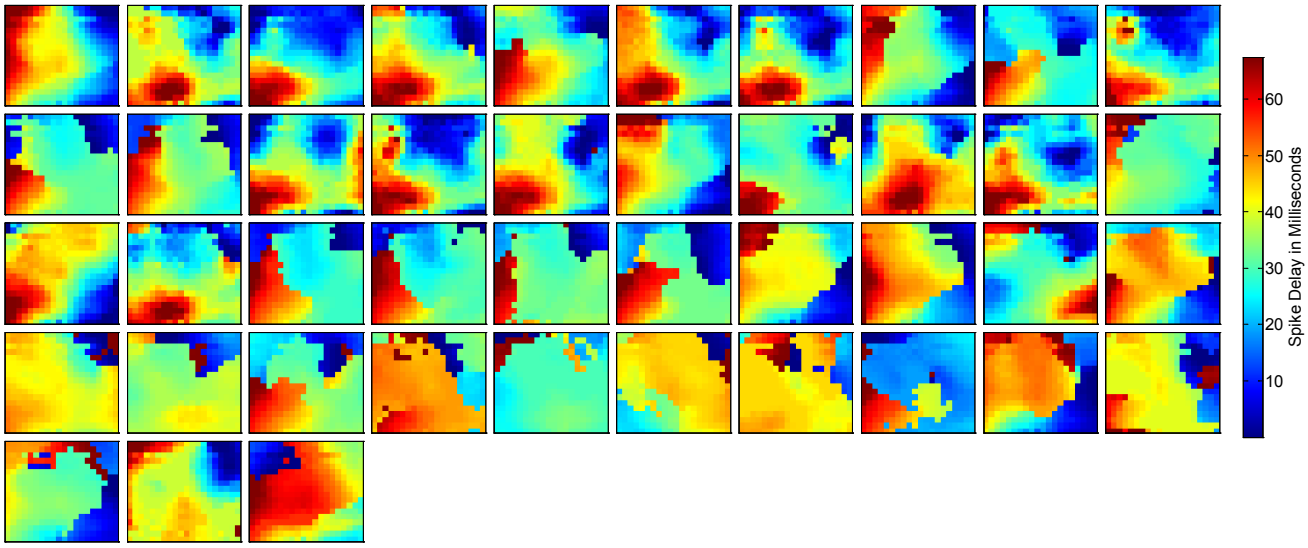

b

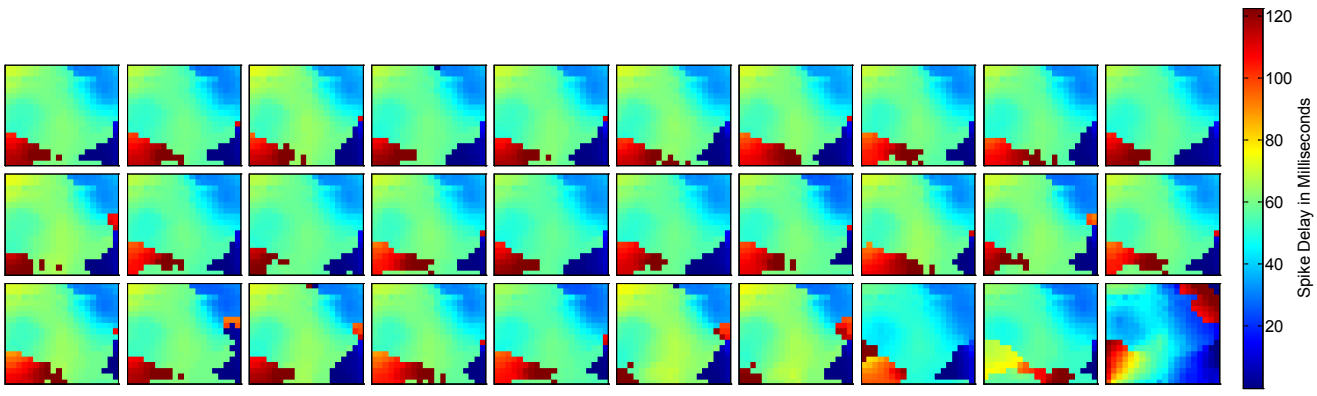

Supplementary Figure 10. Delay maps for all of the spikes in each cluster indicated a strong similarity within clusters. The spikes in clusters 2, 4, 12, 14, and 19 appeared to occur almost exclusively during seizures, while spikes in the other clusters appeared to occur uniformly throughout the record.

a

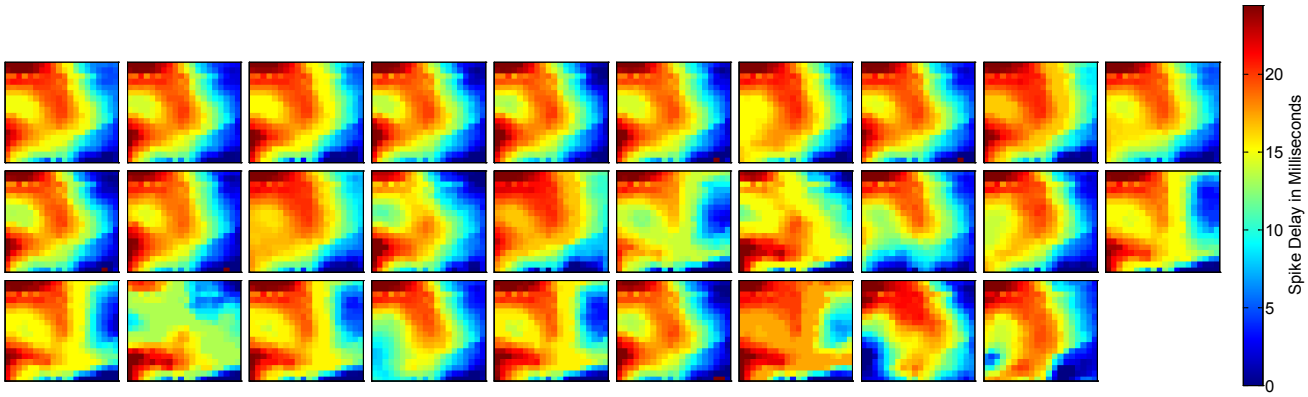

b

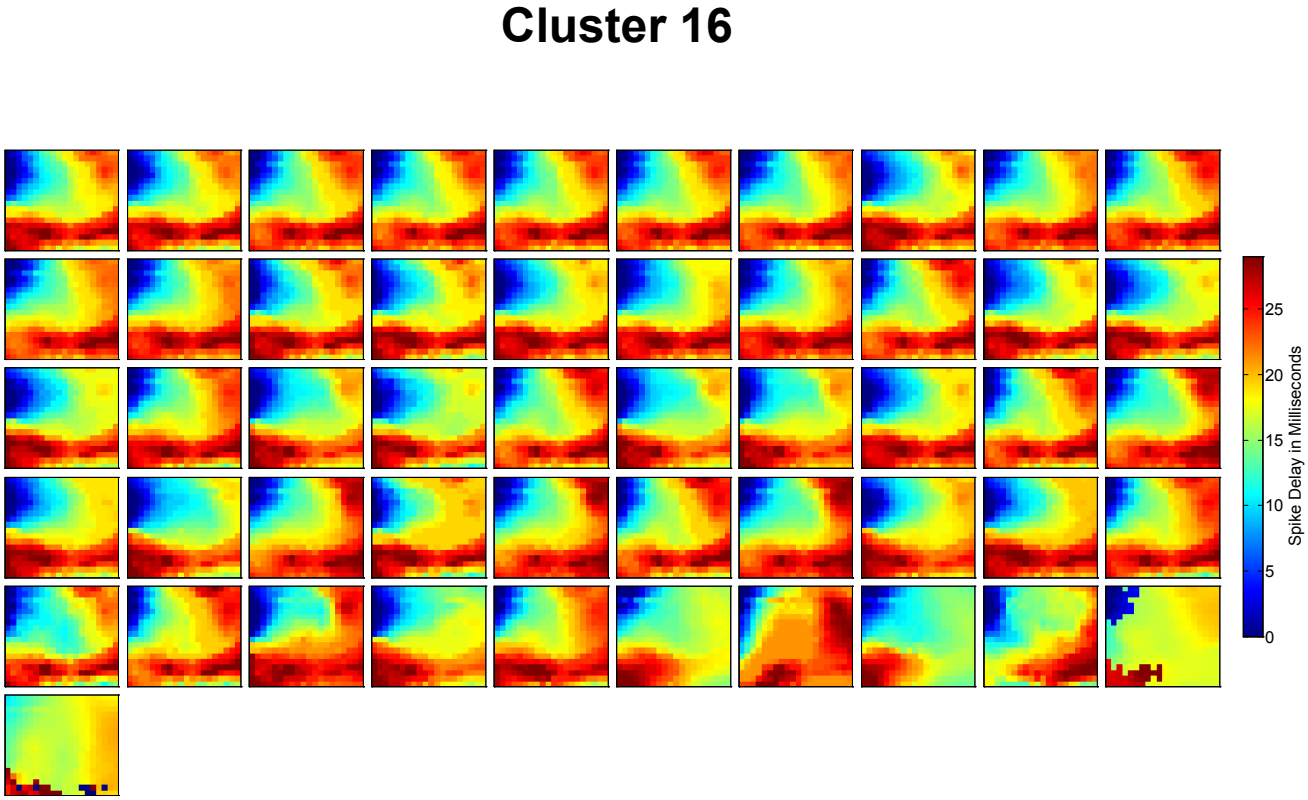

Supplementary Figure 11. Delay maps for all of the spikes in each cluster indicated a strong similarity within clusters. The spikes in clusters 2, 4, 12, 14, and 19 appeared to occur almost exclusively during seizures, while spikes in the other clusters appeared to occur uniformly throughout the record.

a

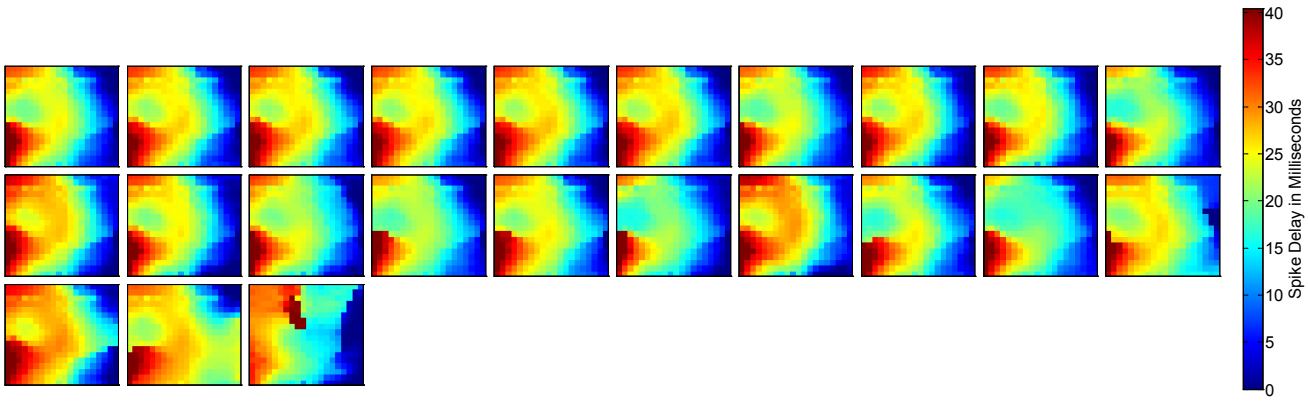

b

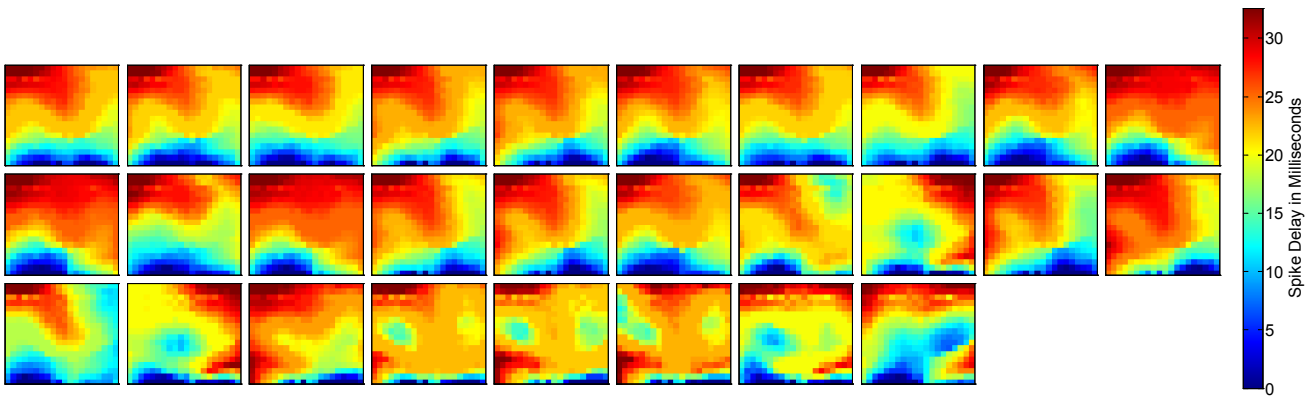

Supplementary Figure 12. Delay maps for all of the spikes in each cluster indicated a strong similarity within clusters. The spikes in clusters 2, 4, 12, 14, and 19 appeared to occur almost exclusively during seizures, while spikes in the other clusters appeared to occur uniformly throughout the record.

a

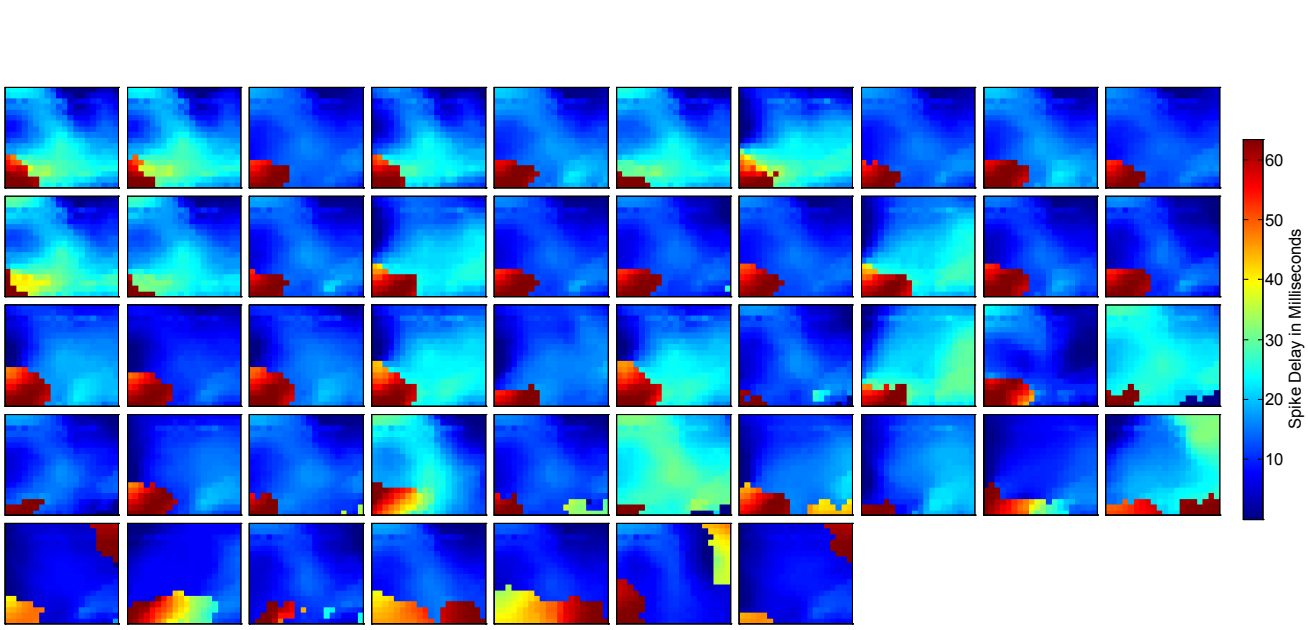

b

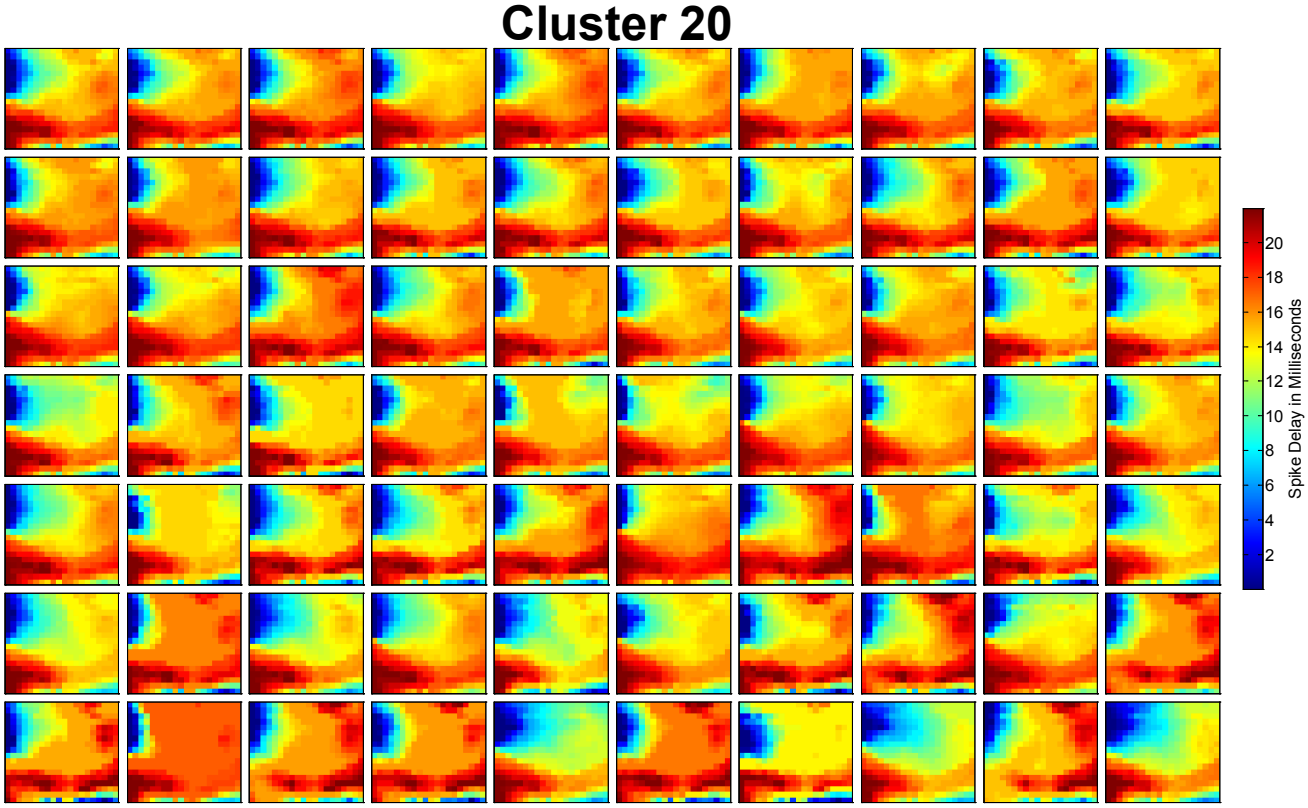

Supplementary Figure 13. Delay maps for all of the spikes in each cluster indicated a strong similarity within clusters. The spikes in clusters 2, 4, 12, 14, and 19 appeared to occur almost exclusively during seizures, while spikes in the other clusters appeared to occur uniformly throughout the record.

a

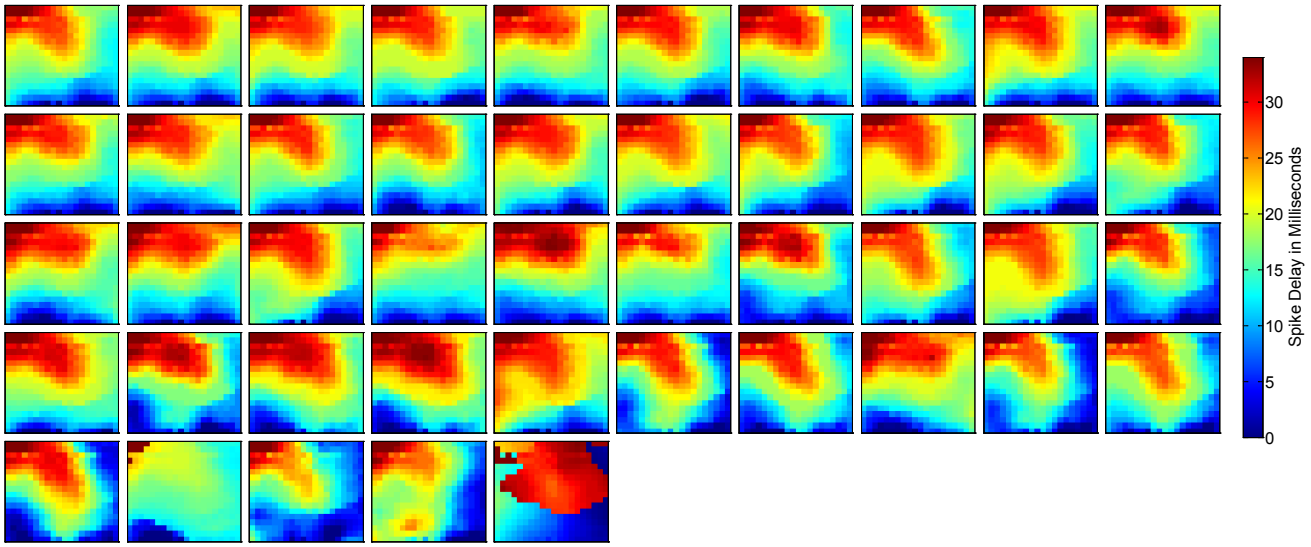

Supplementary Figure 14. Delay maps for all of the spikes in each cluster indicated a strong similarity within clusters. The spikes in clusters 2, 4, 12, 14, and 19 appeared to occur almost exclusively during seizures, while spikes in the other clusters appeared to occur uniformly throughout the record.

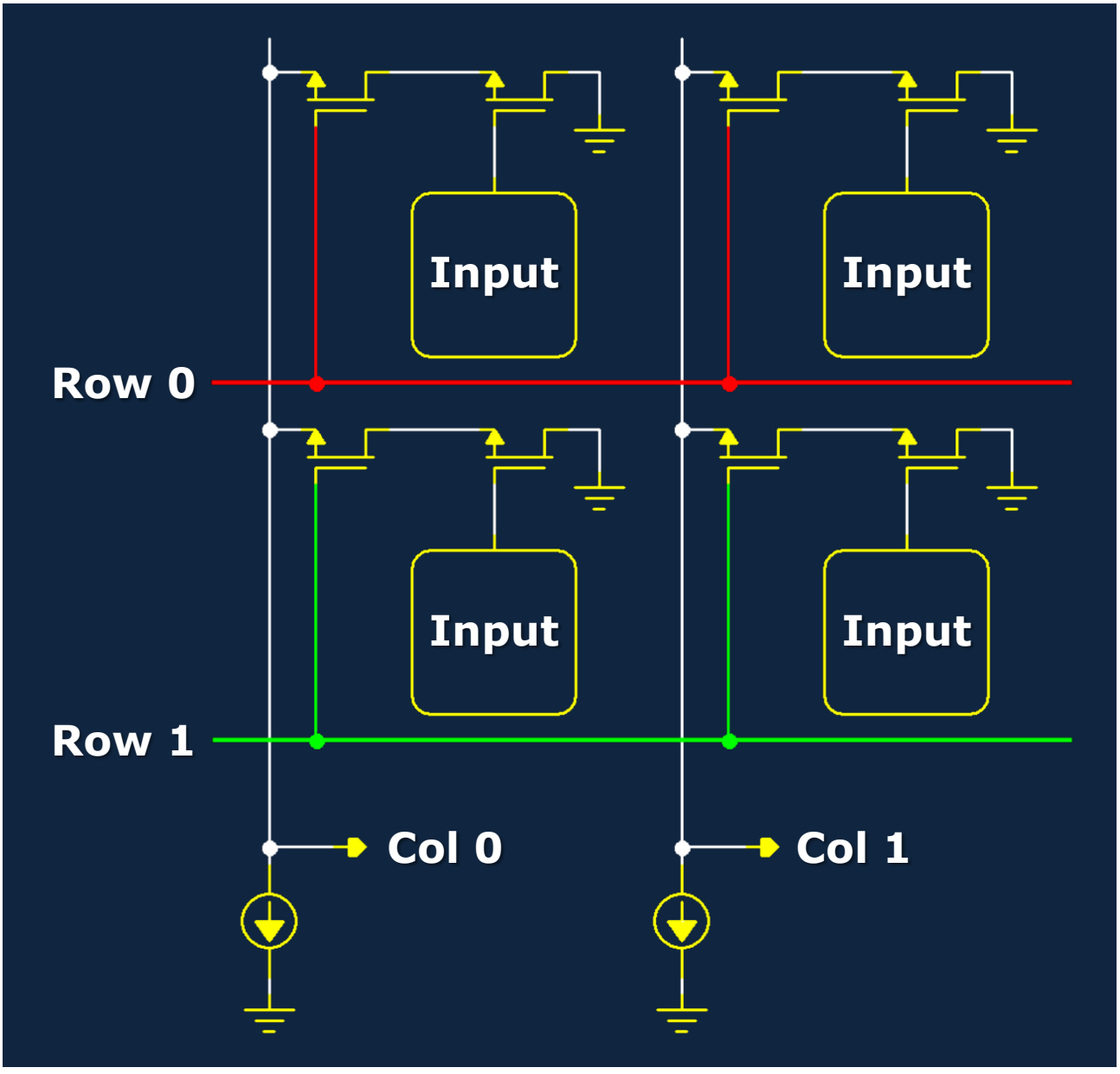

Supplementary Figure 15. Circuit diagram of four unit cells, showing multiplexing connections.

a

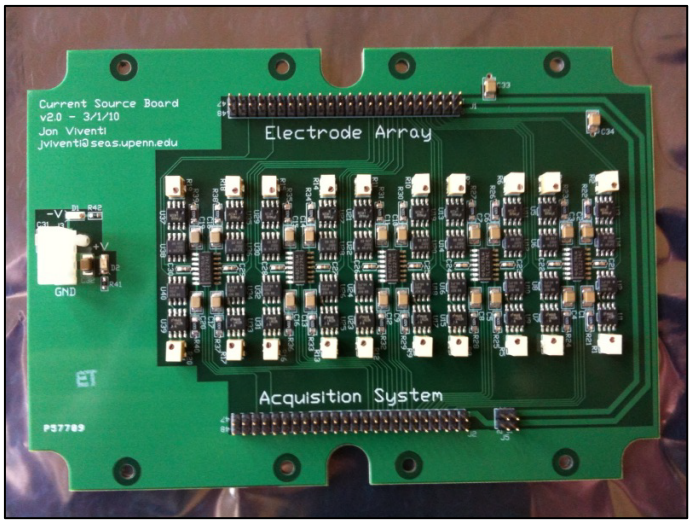

b

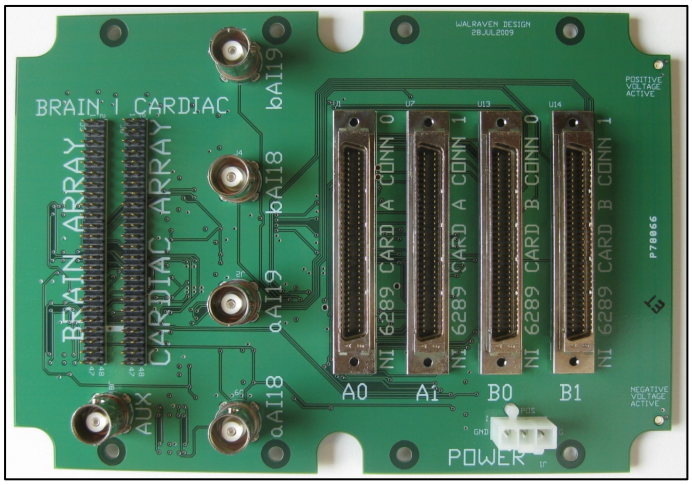

c

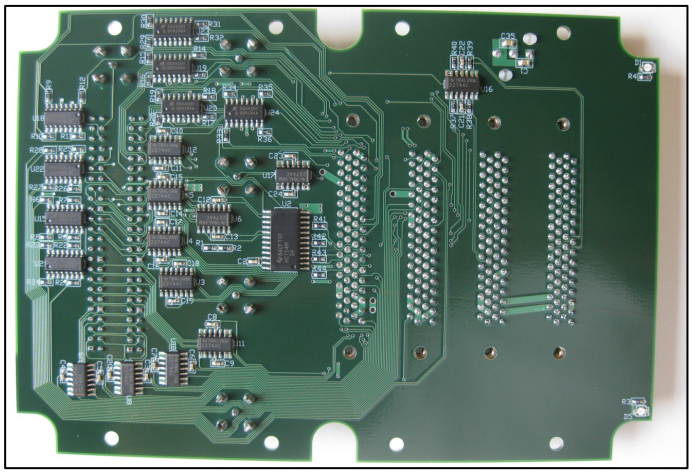

Supplementary Figure 16. Photographs of data acquisition system components. **a,** Photograph of custom circuit board that implements the off array constant current sinks, buffering and high-pass filtering. **b,** Photograph of custom data acquisition interface circuit board that generates row select signals and provides another stage of buffering (top) and **c,** (bottom).

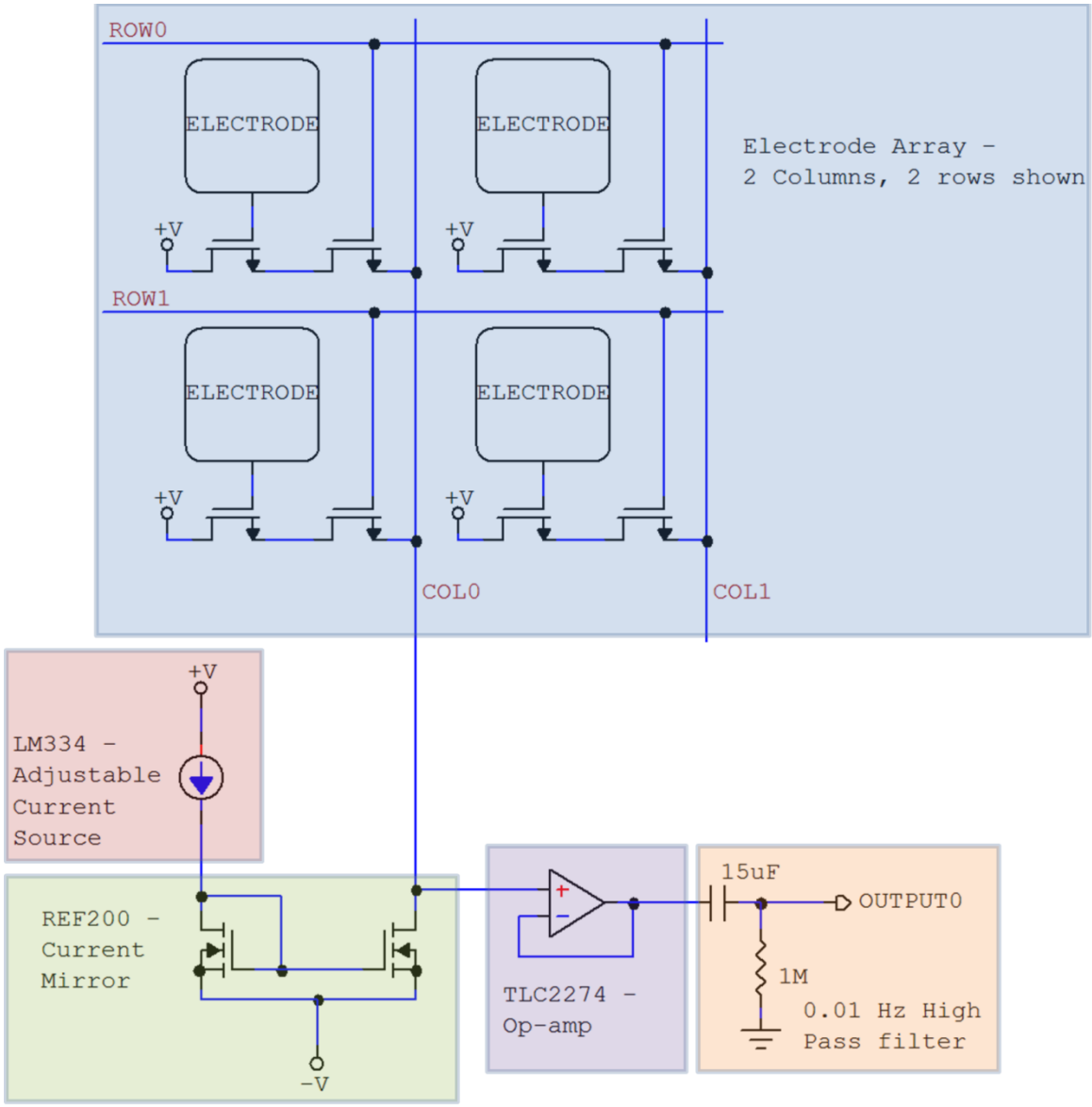

Supplementary Figure 17. Block diagram of constant current sink implementation. This circuit is repeated 20 times, one for each column of the electrode array.

Supplementary Figure 18. Complete schematics of the custom data acquisition interface circuit board.

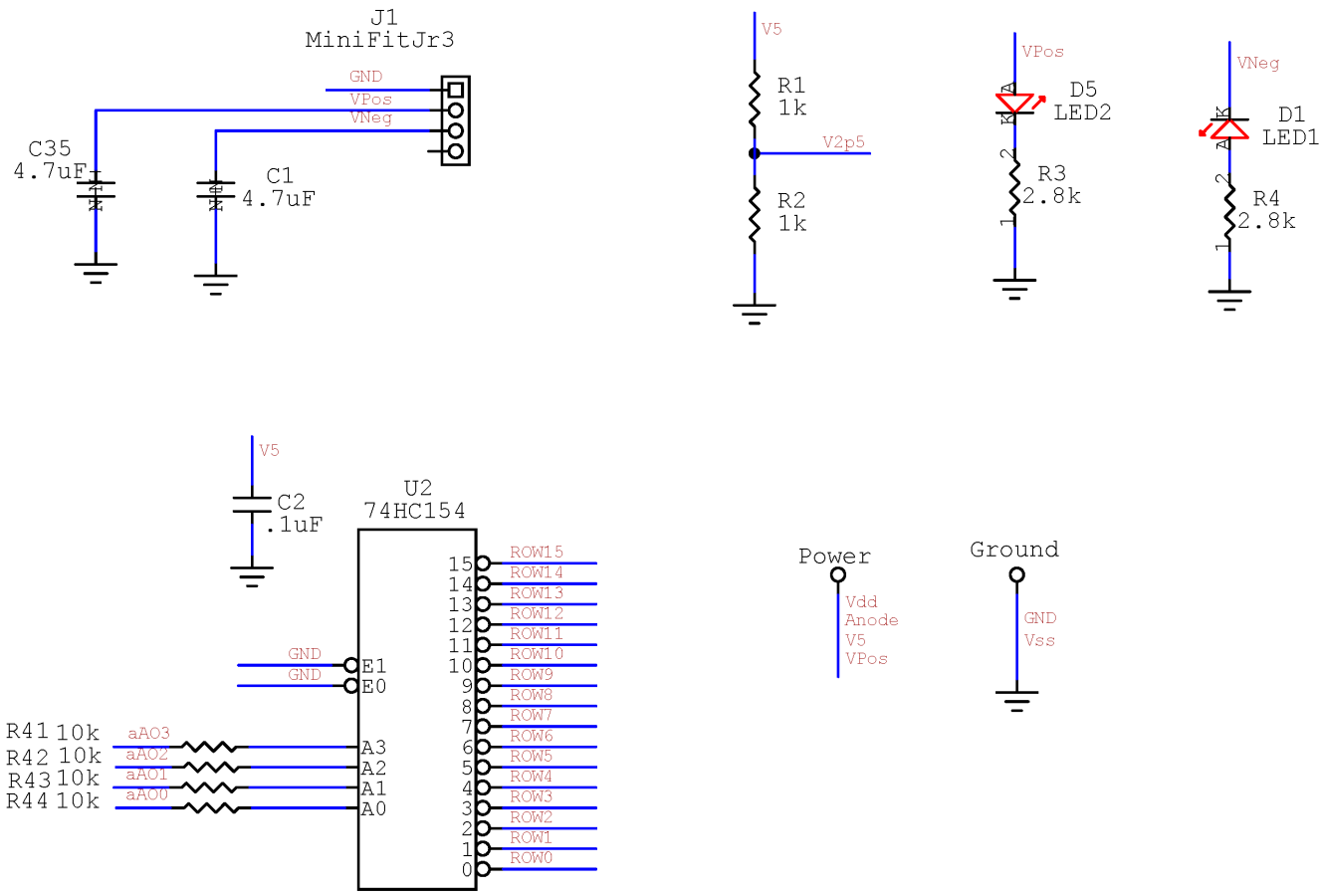

Rev	ID
1.0	Active Electrode Interface Board
Date: 11/4/08	Page: 1 of 8

Supplementary Figure 19. Complete schematics of the custom data acquisition interface circuit board.

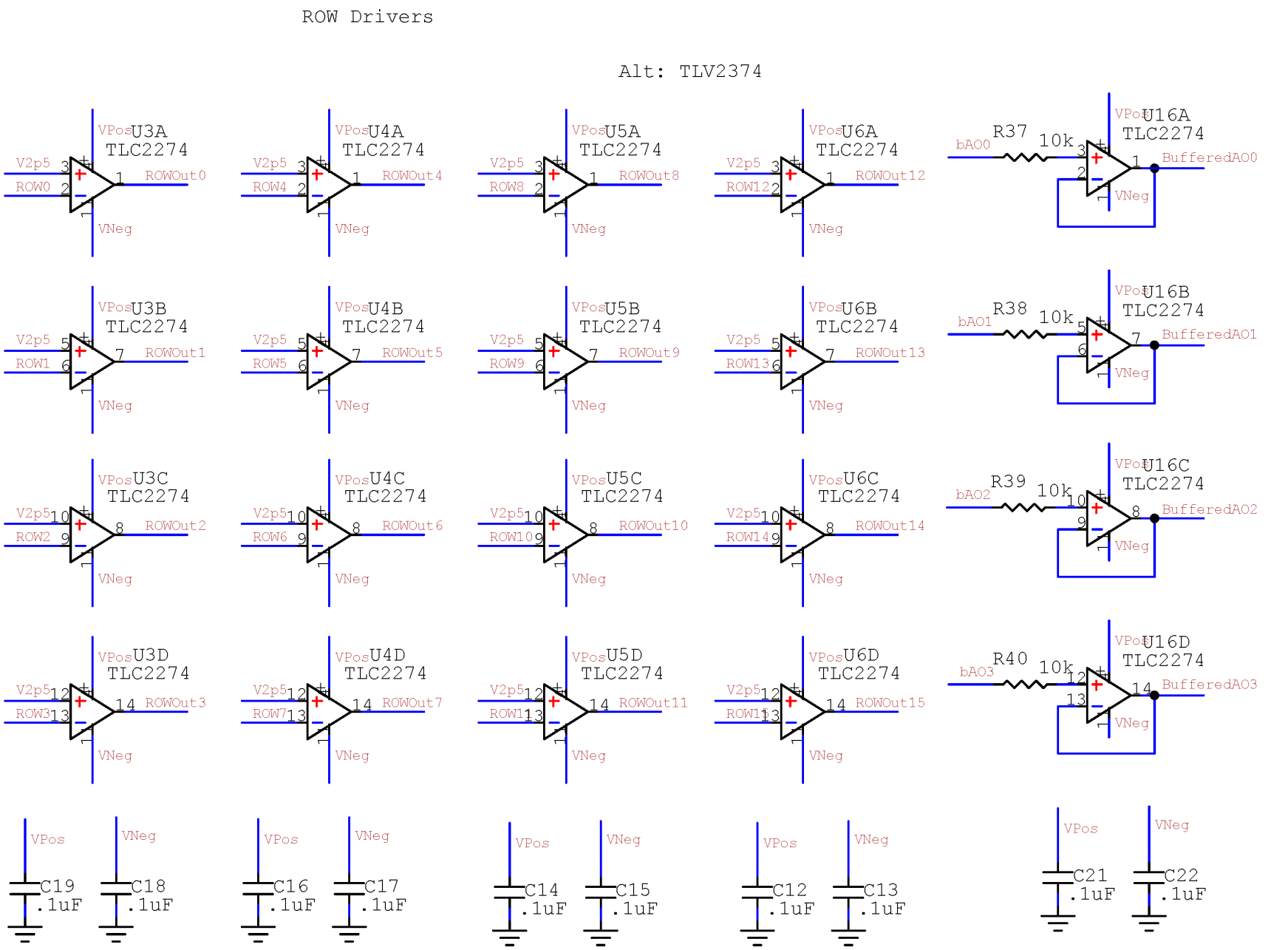

Rev	ID
1.0	Active Electrode Interface Board
Date: 11/4/08	Page: 2 of 8

Supplementary Figure 20. Complete schematics of the custom data acquisition interface circuit board.

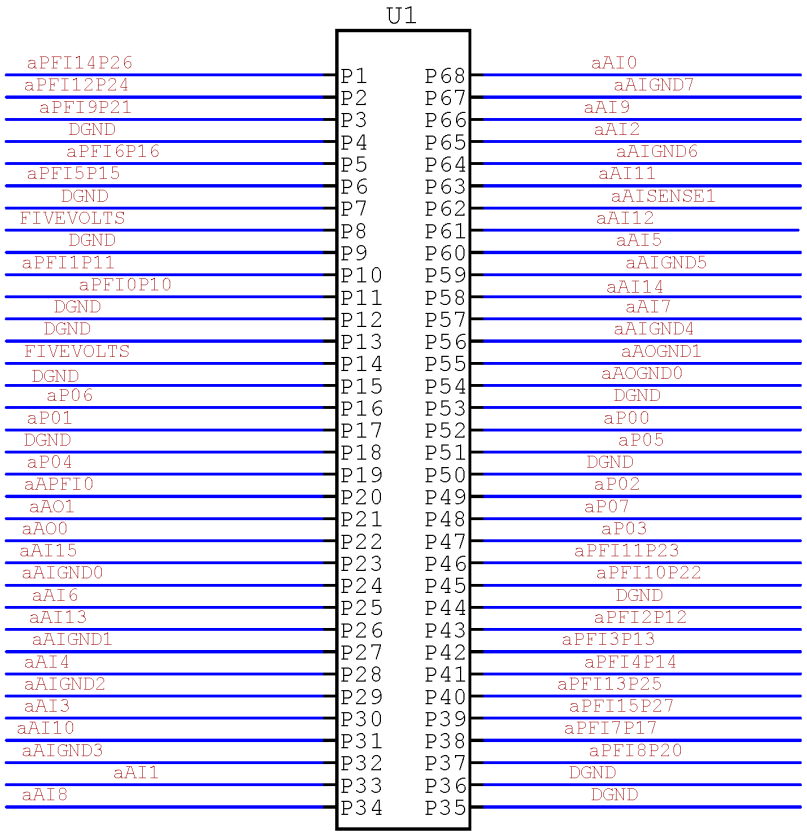

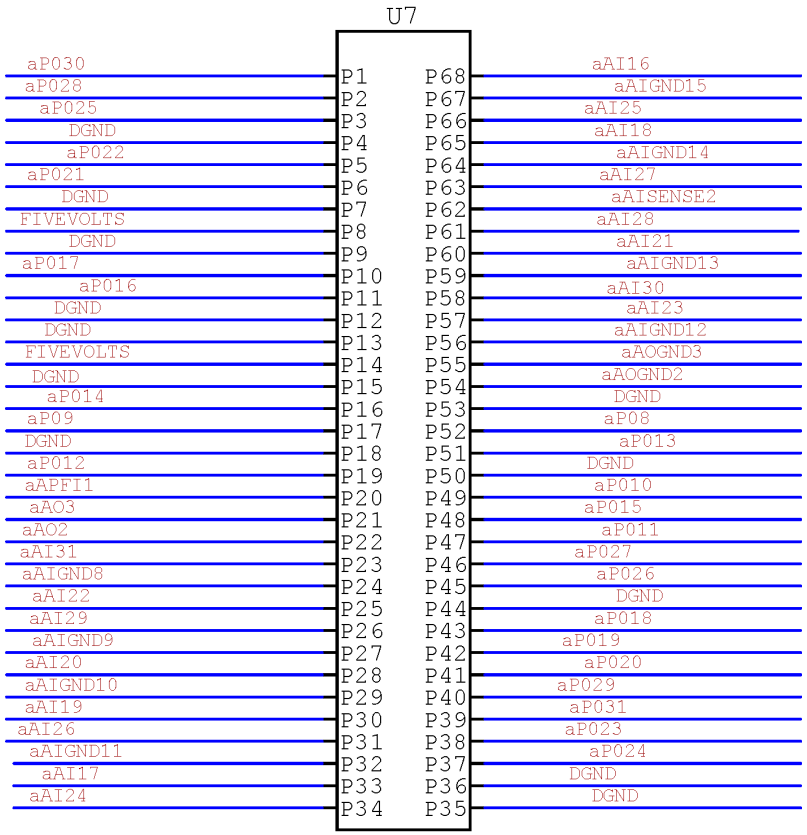

Rev	ID
1.0	Active Electrode Interface Board
Date: 11/4/08	Page: 3 of 8

Supplementary Figure 21. Complete schematics of the custom data acquisition interface circuit board.

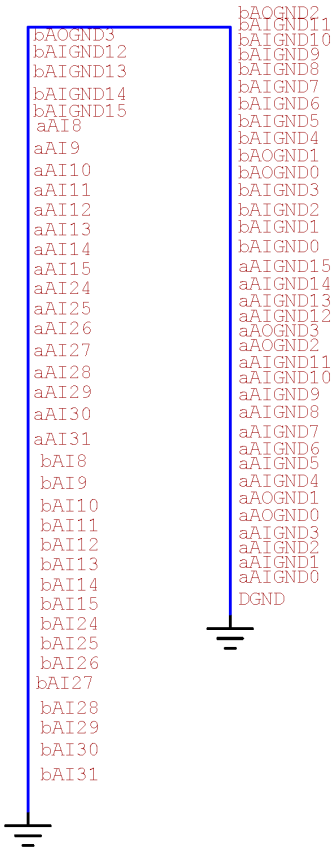

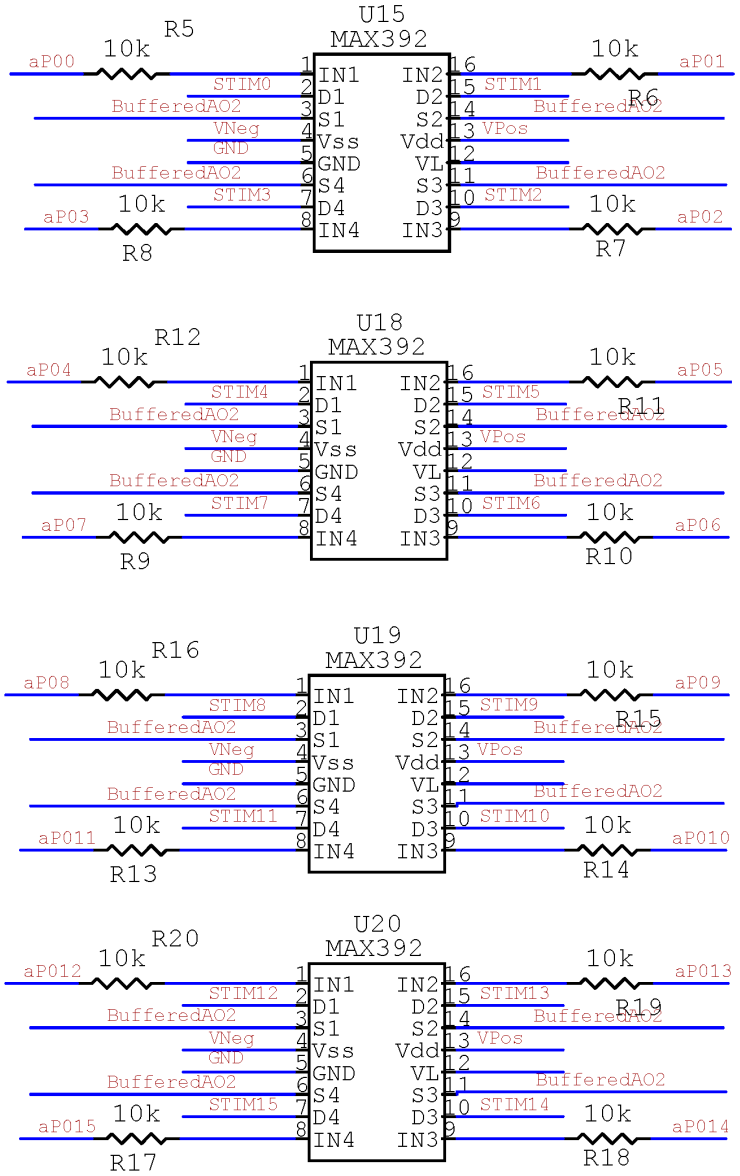

Rev	ID
1.0	Active Electrode Interface Board
Date: 11/4/08	Page: 4 of 8

Supplementary Figure 22. Complete schematics of the custom data acquisition interface circuit board.

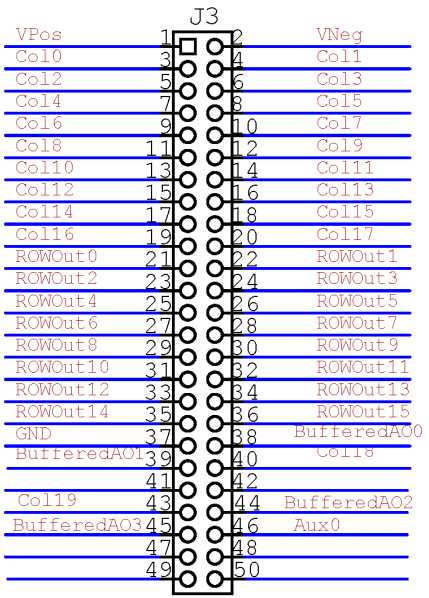

Molex 15-91-0400

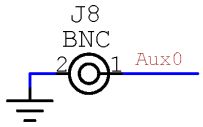

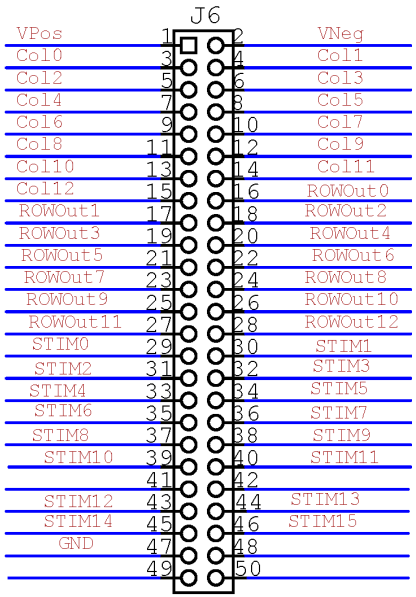

Rev	ID
1.0	Active Electrode Interface Board
Date: 11/4/08	Page: 5 of 8

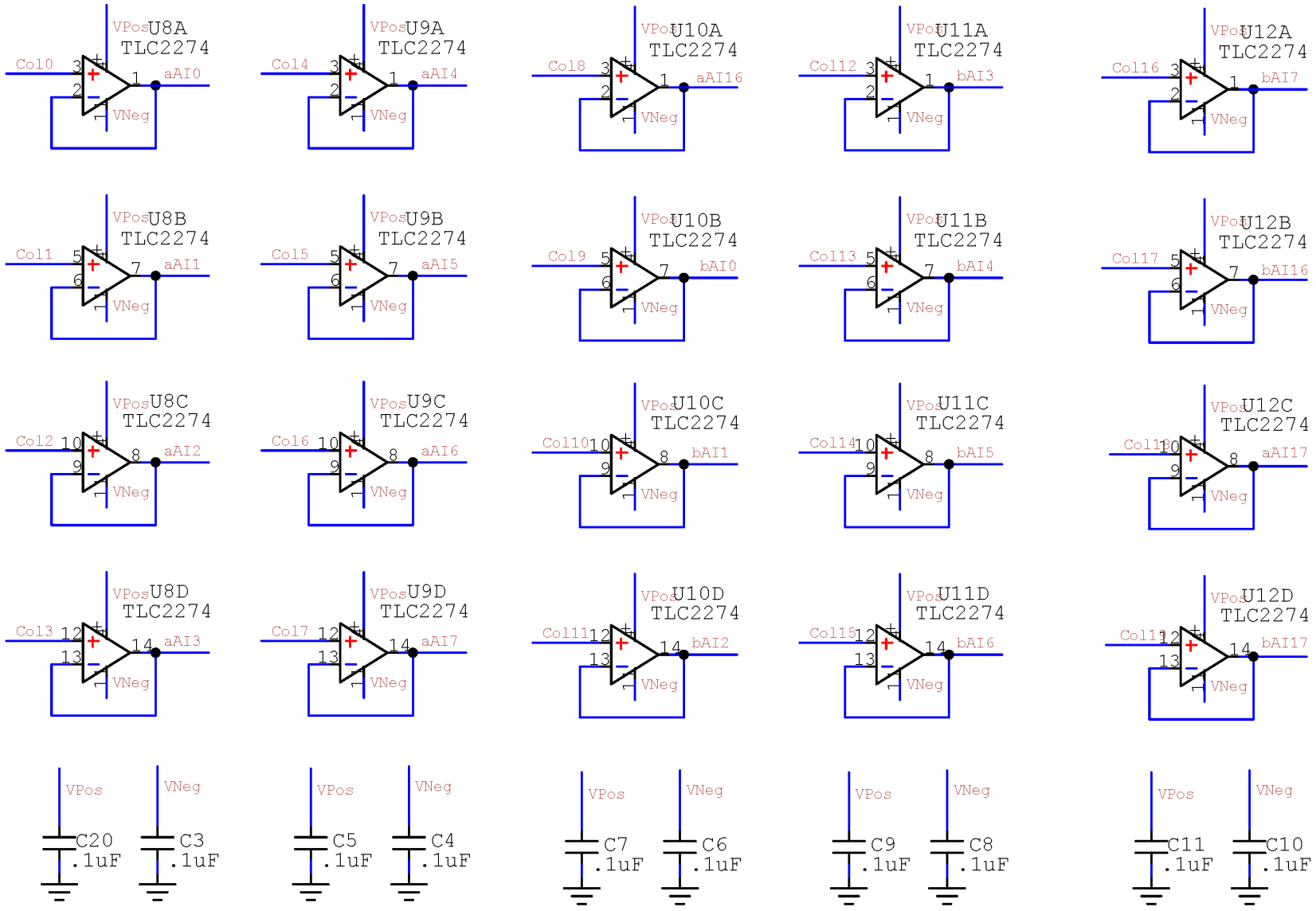

Rev	ID
1.0	Active Electrode Interface Board
Date: 11/4/08	Page: 6 of 8

Supplementary Figure 23. Complete schematics of the custom data acquisition interface circuit board.

Supplementary Figure 24. Complete schematics of the custom data acquisition interface circuit board.

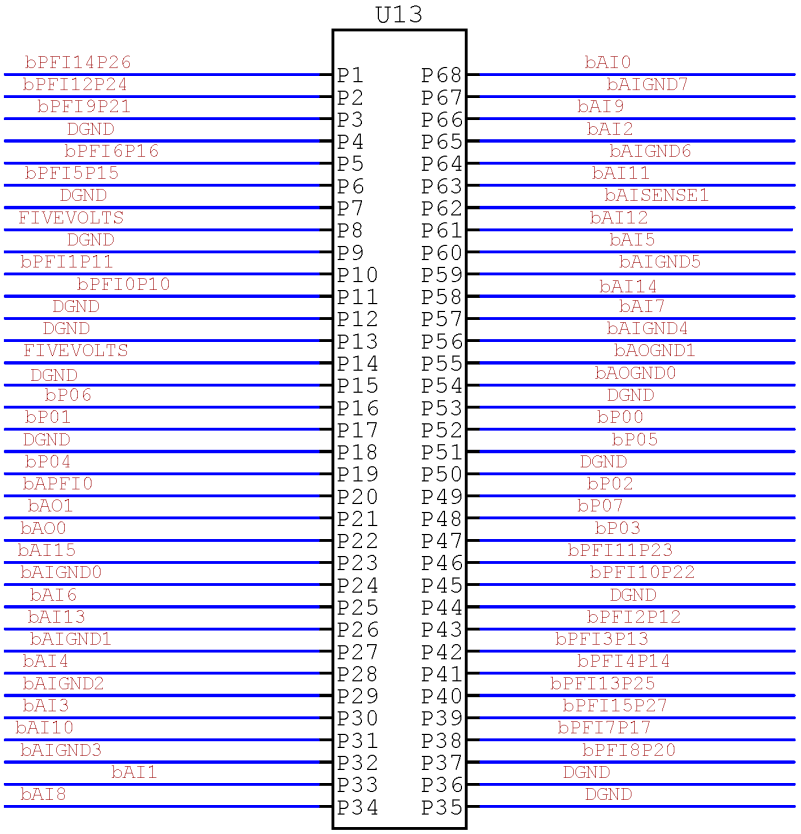

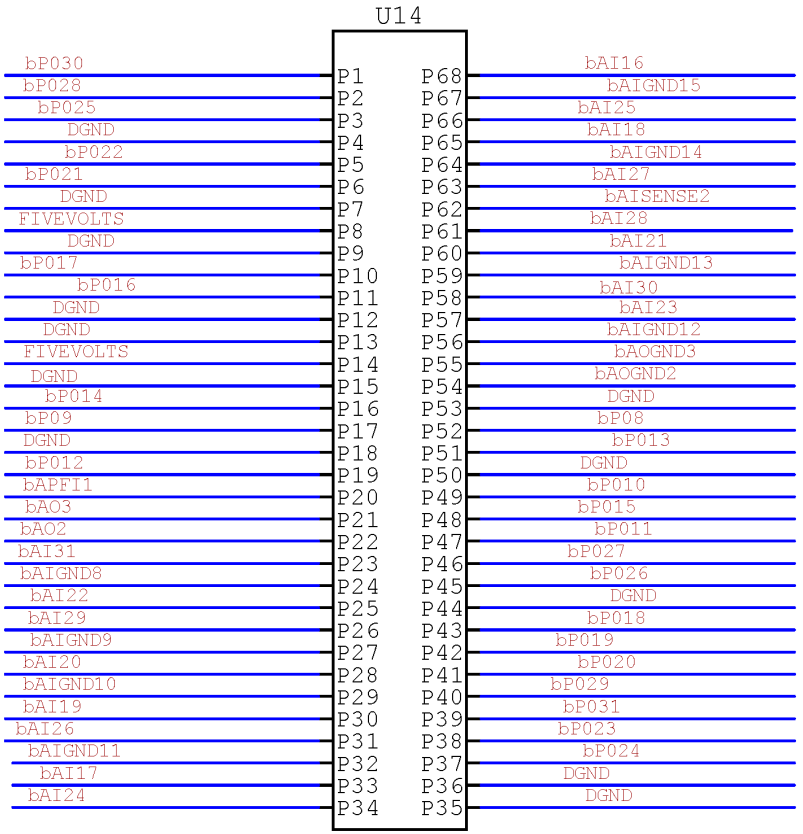

Rev	ID
1.0	Active Electrode Interface Board
Date: 11/4/08	Page: 7 of 8

Supplementary Figure 25. Complete schematics of the custom data acquisition interface circuit board.

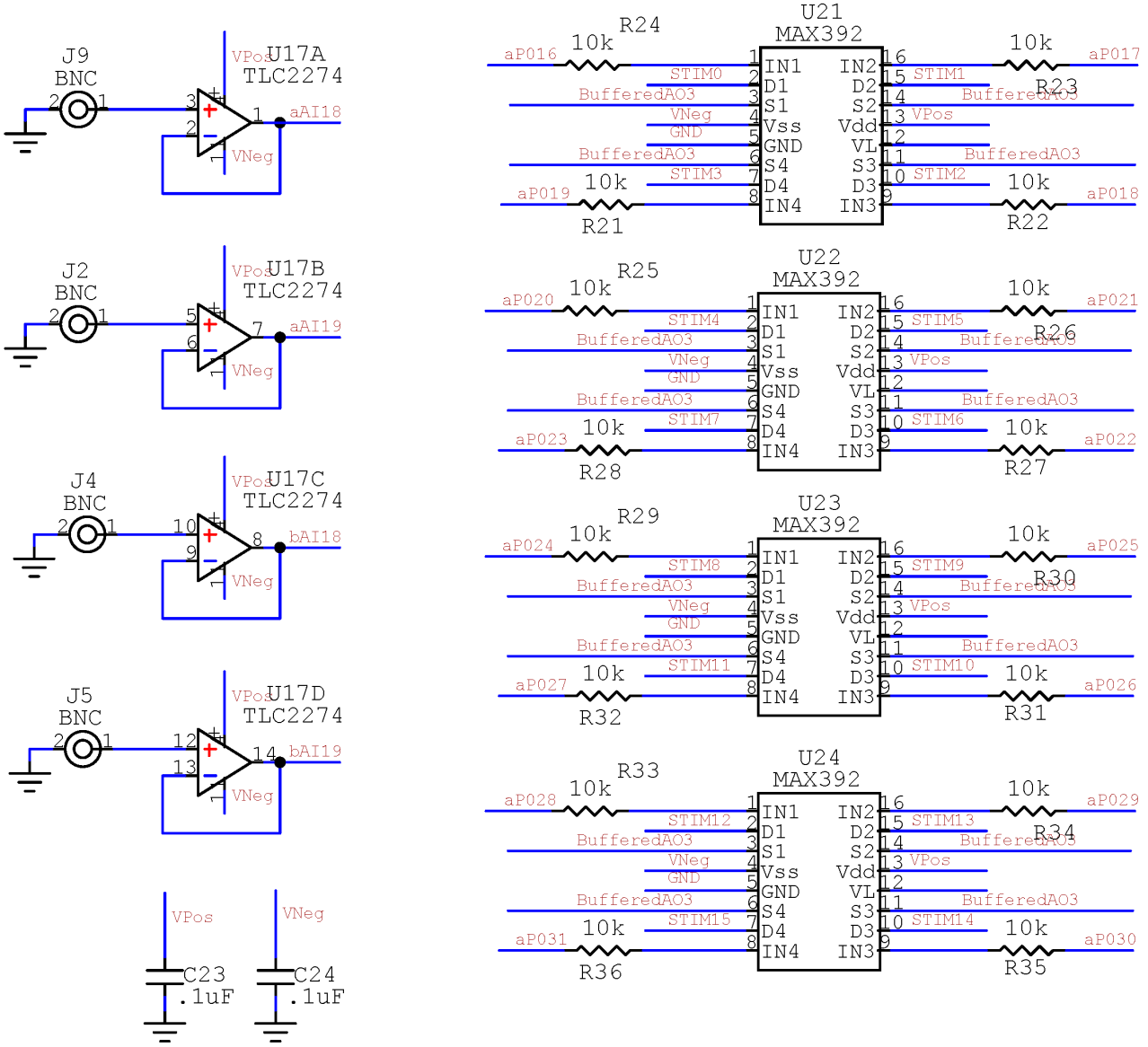

Rev	ID
1.0	Active Electrode Interface Board
Date: 11/4/08	Page: 8 of 8

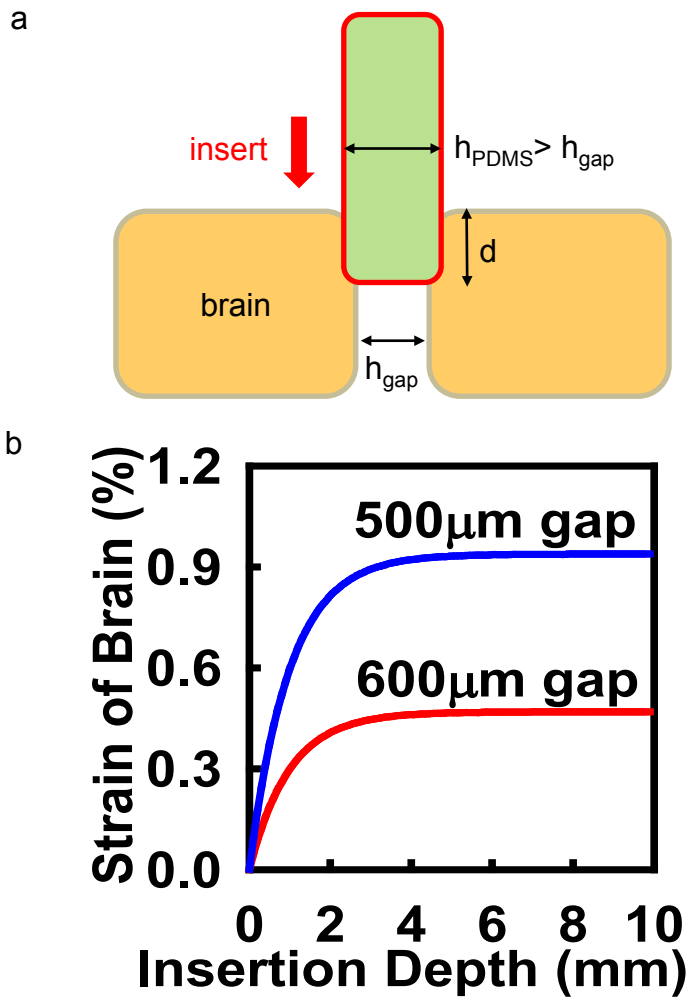

Supplementary Figure 26. Folded electrode mechanical modeling results. **a,** A diagram that shows parameter definitions for insertion model of folded electrode array. **b,** Strain induced in the brain during insertion of the folded electrode array for two different brain hemisphere spacings.

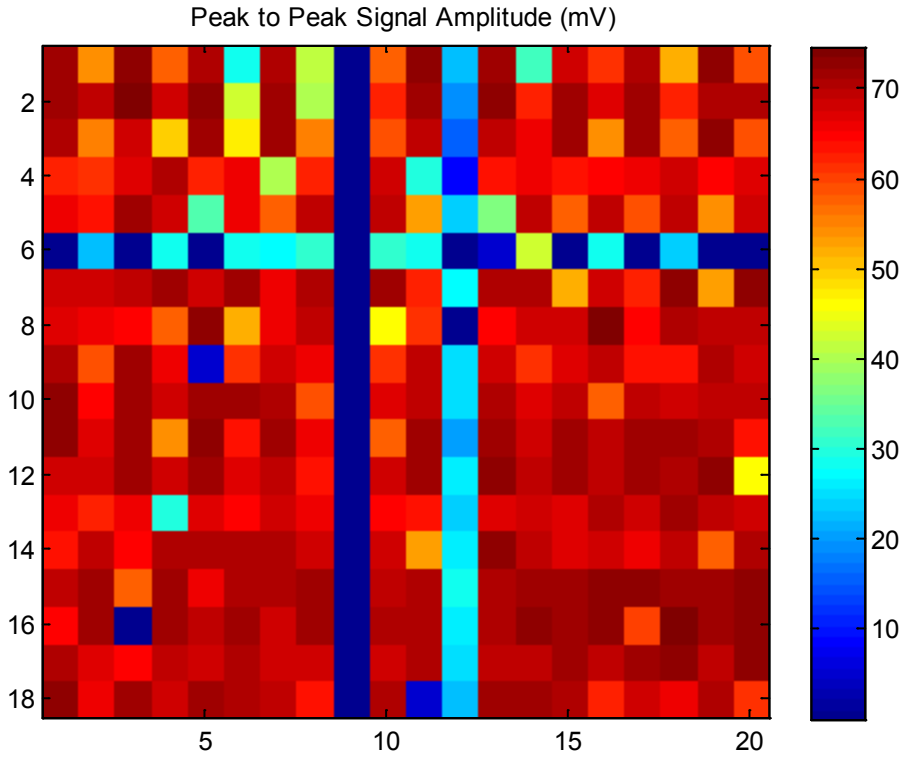

Supplementary Figure 27. Color map illustrating the spatial distribution of the electrode response to a 100mV p-p, 3.14 Hz sine wave, demonstrating the spatial uniformity of the gain of the electrode array.